University of Cape Town

Doctoral Thesis

Axial Segregation of Granular Flows in Rotating Drums

Author:
Elbasher M E Ahmed

Supervisor:
Prof Indresan Govender

A thesis submitted in fulfilment of the requirements for the degree of Doctor of Philosophy

in the

Department of Physics, Faculty of Science
University of Cape Town

October 2017

Declaration of Authorship

I, Elbasher Mohamed, declare that this thesis titled, ' Axial Segregation of Granular Flows in Rotating Drum' and the work presented in it are my own. I confirm that:

- This work was done wholly or mainly while in candidature for a research degree at this University.
- Where any part of this thesis has previously been submitted for a degree or any other qualification at this University or any other institution, this has been clearly stated.
- Where I have consulted the published work of others, this is always clearly attributed.
- Where I have quoted from the work of others, the source is always given. With the exception of such quotations, this thesis is entirely my own work.
- I have acknowledged all main sources of help.
- Where the thesis is based on work done by myself jointly with others, I have made clear exactly what was done by others and what I have contributed myself.

Signed: Signed by candidate

Date:

"The sand in the hourglass runs from one compartment to the other, marking the passage of moments with something constant and tangible. If you watch the flowing sand, you might see time itself riding the granules."

Vera Nazarian

UNIVERSITY OF CAPE TOWN

ABSTRACT

Faculty of Science
Department of Physics

Doctor of Philosophy

Axial Segregation of Granular Flows in Rotating Drums

by: Elbasher Mohamed Elbasher Ahmed
Centre for Minerals Research
University of Cape Town - Private Bag X3, Rondebosch, 7701, South Africa

A mechanistic model of axial segregation in rotating drums is presented for mixtures of granular material. We show that grains composed of different material properties—which are heuristically argued to manifest as differences in frictional properties at the continuum scale—diffuse into axial bands as a consequence of concentration fluctuations in the free surface layer caused by friction-limited mobility. The model is composed of two new ingredients that successfully recover the well-known phenomenon of axial banding and subsequent band coarsening in the long-time evolution: (1) A Bagnoldian stress assumption facilitated band formation at drum fill levels $< 50\%$, that have hitherto not been possible with a Newtonian shear stress ansatz, through the formation of an asymmetric free surface profile that is experimentally verified by the nuclear imaging technique of Positron Emission Particle Tracking. (2) The geometric slope corresponding to the gravity-driven axial flux between adjacent bands is (binomially) expanded to second order thereby ensuring band coarsening in the long-time limit for all boundary conditions investigated. Numerical implementation of the axial diffusion model is shown to be sensitive to the boundary conditions of the tumbling mill (particle size, volume concentration, mill speed, average friction, end wall friction, drum length and drum diameter). The explicit solutions for a binary-, ternary-, quaternary- and n-species granular mixture was developed with numerical implementation up to $n = 4$. Consistent with experimental observations in the literature, the 3-species mixture successfully captures bands within bands, while the 4-species mixture successfully recovers bands within bands, within bands.

Acknowledgements

Foremost, I want to offer this endeavor to Allah Almighty who always gives us uncountable favours.

I would like to express my deepest appreciation and sincere thanks to my supervisor Professor Indresan Govender. I am very grateful to Professor Govender for his unwavering support and for the interesting discussions, suggestions, insightful feedback and comments.

It is my pleasure to thank the academic and administrative staff of the Physics Department, University of Cape Town, for their assistance during my study.

I wish to thank my colleagues of the Applied Physics Research Group for their moral and technical support.

This work was financially supported by the Centre for Minerals Research (CMR).

Finally, I would like to thank my family, my parent, my wife, my lovely son Mohamed, my brothers and my sisters for their support, love and encouragement.

Contents

List of Figures

List of Tables

Symbols

Symbol	Meaning
a	the volume fraction
a_z	the axial surface curvature on the axial plane
C	the relative concentration
D_{coef}	the diffusion coefficient
d	the grain size
g	gravity (9.8 m/s^2)
h or x_0	free-surface thickness
W	the length of the drum
n_d	the number density of granular media
R	the inner radius of the drum
ϕ	the volume concentration
η	the viscosity of grain media
λ	the linear concentration profile according to Bagnold
ρ	the density of granular material
μ	the average or bulk friction coefficient
μ_b	the basal friction coefficient
μ_i	the inter-particle friction coefficient
μ_w	the wall friction coefficient
ω	the angular velocity of the rotating drum (rotation rate)
Θ	the dynamic angle of repose

For my mother Um Elhassan Mohey Eldin, my father Mohamed Elbasher, my wife Smah Alsed, my brothers and sisters and my sweet lovely son Mohamed. I love You all so much.

Chapter 1

Introduction

1.1 Granular Materials

In our daily lives, if you enter your kitchen you may see rice or sugar, and if you pass along a beach you may observe children playing with piles of sand; you will also find some medicines in the form of grains if you go to a pharmacy and, in some countries, during the winter season, you can watch a natural avalanche of ice. All these materials (rice, sugar, sand, etc) - see Fig. 1.1 - are examples of the so-called ***granular materials***, which are ubiquitous. Granular materials are extremely common in nature, in our food, as well as in industry such as mining, pharmaceutical, chemical and agricultural processes. Granular material

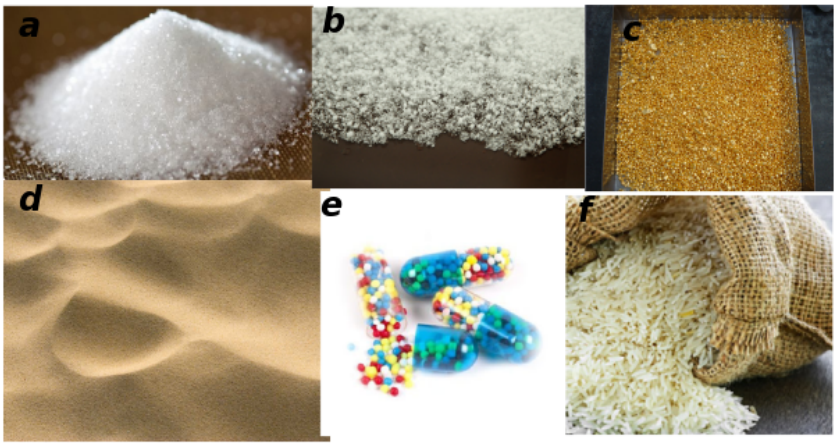

FIGURE 1.1: Different samples of granular materials: (a) sugar, (b) ice grains, (c) granular gold, (d) sand, (e) pharmaceutical grains, and (f) rice.

is an assemblage and conglomeration of a large number of discrete solid particles,

and, as presented in Section 1.1.1, granular material can be found in almost all phases of matter.

In terms of size, particles can be considered granular materials if they have a size d that is larger than one micron. This lower size-limit (1 μm) is the boundary between granular particles and Brownian particles as, below this limit, thermal agitation is important and Brownian motion can be seen [1]. That implies that grains are collections of macroscopic particles, as, for example, the size of a grain of sand can be in the range of a few to several hundred microns.

1.1.1 Classification

Granular materials can be broadly classified into three states that closely resemble the three common states of matter (solid, liquid and gas). The granular solid state can simply be observed when granular particles form a pile in a container [2]. In this case, the particle interactions are dominated by the plastic solid interactions with a finite yield stress. Sufficient tilting of the container causes the granular material to flow like a fluid, as commonly observed in heap [3] or rotating drum flows [4, 5]. In this case, the surface layer (***free-surface layer***) of particles flows atop a (near static) bed of particles. The free surface profile described in Chapter 2 provides a key input to the segregation mechanisms developed in this thesis. In the liquid-like state, the behavior of flows is dominated by the viscous hydrodynamic laws. The gas state can be seen when strong agitation is applied to the grains' container. In this case, the grains interact mainly through collisions with each other and the container walls. In rotating drums the free-flight or cataracting mode exhibits such gas-like features.

The Groupement De Recherche Milieux Divisès (GDR MiDi) [4] classified granular materials according to the flow velocity of the following regimes:

The quasi-static regime:

Grain inertia is negligible. The material is often described using soil plasticity models.

The gaseous regime:

It exists when the medium is strongly agitated and the grains are far apart from one another. In this regime, particles interact through binary collisions and a kinetic theory has been developed by analogy with the kinetic theory of gases.

The dense flow regime:

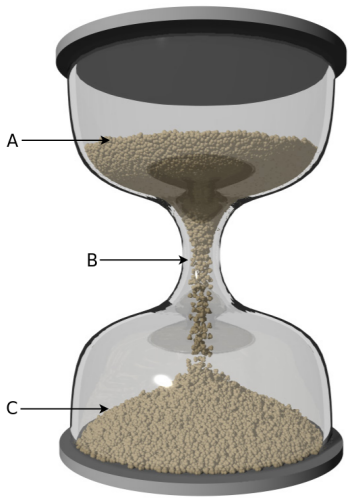

FIGURE 1.2: Different regimes of granular material. (A) solid, (B) liquid, and (C) gas. The original photo was taken from Ref. [6].

Between these two regimes, there exists a dense flow regime where grain inertia becomes important but where a contact network still exists that percolates through particles.
The most common two phases that granular materials display are the solid phase and the liquid phase. The transition between these two phases is observed through many different phenomena, such as avalanches, surface flows, sliding and stick-slip.

1.1.2 Difficulties Encountered in the Study of Granular Materials

There are many difficulties that are encountered in the study of granular flows:

1. The calculations corresponding to granular material are very difficult and complicated because of the dissipative nature of the particle interactions. The dissipative (shear and compressive) contact interactions, including friction and inelastic collisions, lead to non-linear calculations.

2. The second difficulty arises from the fact that particles are too large to undergo Brownian motion and the statistical average over different configurations is not possible.

3. Another difficulty lies in the coexistence of both liquid and solid behaviours of the material, as observed in heap and rotating drum flows [3, 5, 7].

4. In terms of computer simulation, granular material contains a large number of particles. A spoon of sugar, for example, contains more than one million grains [8], which need a powerful (super) computer to simulate their motions and flows. The problem becomes worse when we consider that tumbling mills—the industrial application of rotating drum flows—contain $\sim$ a billion particles.

5. To date, there is no clear scale-separation between the size of grains and the size of the flow (system size) [9].

6. One of the serious difficulties is the storage, transport and handling of granular materials [10], which range from undesired clogging, through unwanted mixing or segregation, to the structural collapse of silos (Fig 1.3).

FIGURE 1.3: Silo Collapse. Photo taken from Silo failure video (https://www.youtube.com)

7. It is quite difficult to extract common features and general trends for granular flows as configurations used to study the characteristics of granular flows are not the same, as well as experimental or numerical conditions varying from one study to another [4].

8. The scaling between the results obtained from the measurements in the laboratory and the actual behavior of the granular materials in the production process represents a difficult transition [2].

1.2 This work

The present study forms part of a larger project to develop axial transport models of granular and slurry material in tumbling mills. Unfortunately, little to no fundamental understanding underpins the largely empirical models currently used to control industrial tumbling flows. Accordingly, this research constitutes the first practical steps towards axial flow of granular material in typical[1] configurations of tumbling mills.

1.3 Hypothesis formulation

Two competing theories have been proposed in the physics literature to account for the band formation and subsequent band coarsening in the long time limit. The first theory [7] argues that friction ultimately drives an axial diffusion process which results in the well-observed banding pattern. Unfortunately, the choice of a Newtonian stress-based model with a linear axial gradient fails to recover the experimentally observed:

1. band formation for drum fillings $< 50\%$, and
2. band coarsening in the long time limit.

Clues to the failure are discussed by [11] and relate to the free surface profile being "too highly symmetric". We further assert that linear axial gradients lose sensitivity to surface variations as the diffusion process evolves, causing premature termination of the diffusion process that ultimately results in no band coarsening.

A second theory [12] argues that transient travelling waves seed the early stages of axial banding and a slow logarithmic coarsening of the bands with time. While this theory matches experimental observations, it lacks a physical and practical connection to the engineering world. We thus favour the friction hypothesis and modify it to successfully predict both the banding and subsequent coarsening across a wider range of operating conditions than reported in the literature.

[1] Industrial tumbling mills are operated at fill levels of less than 50% and typically $\sim 30\%$. It is well observed in the literature that current axial segregation models of granular materials fail to produce banding and eventual band coarsening at fillings less than 50%

Differences in a Coulomb-like frictional effect (solid friction) are easily argued in terms of particle properties (size, shape, density, surface roughness) and the associated microscopic picture as given by the standard Hertz theory. In this regard two important results emerging from the microscopic interpretation guide our reasoning [9].

$$F_T = A\tau_c \text{ and} \tag{1.1}$$
$$F_T = F_N\left(\frac{\tau_c}{H}\right), \tag{1.2}$$

where A is the actual contact area of the interacting particles, F_T the tangential frictional force, H the hardness of the material (a material property) and τ_c the critical shear stress required to break the 'welded' asperities that are squeezed under the normal load F_N to form solid joints.

1. **Shape**: Shaped particles exhibit significantly larger contact areas than, say, spheres and consequently frictional effects are increased according to equation (1.1).
2. **Surface roughness**: Rough surfaces are well known to exhibit higher normal forces (pressures) at the asperities than perfectly smooth surfaces and consequently the tangential frictional effects increase according to equation (1.2).
3. **Size**: Smaller particles exhibit more contacts per unit volume than larger particles and consequently the tangential friction (per unit volume) increases according to equation (1.1).
4. **Density**: Higher density particles exhibit larger normal forces and consequently, frictional effects are increased according to equation (1.2).

With these simple friction-based motivations we hypothesise that:

Granular material composed of different frictional properties diffuse into axial bands due to concentration fluctuations in the Bagnoldian free surface layer caused by friction-limited mobility, and boundary-induced anisotropy in the concentration.

The related sub-hypotheses are:

1. Incorporating a Bagnoldian stress into the free surface modelling will produce an asymmetry in the free surface profile that is necessarily required to initiate banding at fill levels less than 50% of the drum volume.

2. Expanding the axial gradient to higher order will increase sensitivity to the axial diffusion process such that band coarsening is recovered.

1.4 Scope and Outline of the Thesis

Chapter (2) explores a review of the literature. In Chapter (3) we present the calculations of the free-surface profile, its experimental determination using Positron Emission Particle Tracking data, and a parametric study. In Chapter (4) we derive the axial diffusion equations corresponding to both free-surface models (Newtonian and Bagnoldian) and the binomially expanded (to second order) axial gradient operator. We then generalise the resulting diffusion equations to multi-species mixtures with explicit solutions for $n = 2,\ 3,\ 4$ and for $n-$species in general. The result obtained from the large set of parameters affecting the axial segregation process are presented in Chapter (5) along with the discussion. The thesis conclusions constitute Chapter (6).

Chapter 2

Literature Review

2.1 Granular flows

The importance of granular flows is clearly underscored by it's ubiquity. Central to the problem of modelling granular flows as a continuum is the underlying constitutive law. Starting from Bagnold's [13] scaling law through to Savage and Hutter [14], and more recently, Jop et al. [15], a few theoretical and experimentally-derived laws have been proposed. The aim of this review is to highlight the various contributing factors to the mechanism of axial segregation, identify the limitations and successes in current formulations and hence propose a way forward for the research covered in this thesis.

Bagnold [13] showed experimentally that, for non-Brownian motion, the shear stress is proportional to the square of the strain rate. Savage and Hutter [14] successfully developed a model to describe granular flows, which was based on depth-averaged mass and momentum balance equations—the so-called Saint Venant equations.

Jop et al. [15] proposed the first tensorial constitutive relation for surface flows based on a visco-plastic rheology. This model has recently been generalised [16] to include all phases of granular flow. Unfortunately, none of these granular flow models adequately address rotating drum flows. Govender and Pathmathas [5] highlight the complex rheology in tumbling mills, but have yet to develop the constitutive equation consistent with their experimental observations.

2.2 Rotating drums and other geometrical configurations

The world of granular materials is quite interesting as a rich variety of novel and challenging experimental phenomena can be produced using relatively simple equipment [17]. Fig. 2.1 shows the six common flow configurations that are widely used in industry and research laboratories. These flow configurations can be divided into two categories, namely, confined or free surface flows. While the flow in shear cells or silos is confined between walls, the flows down an inclined plane and in a rotating drum fall into the free surface category.

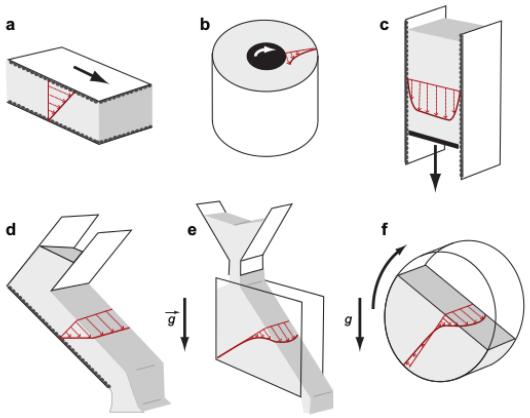

FIGURE 2.1: Different flow configurations: (a) plane shear, (b) Couette cell, (c) silo, (d) flows down an inclined plane, (e) flows on a pile, and (f) flows in a rotating drum [18].

Over the past few decades, rotating drums have attracted numerous research efforts from both engineering and physics communities. The rotating tumbler system has been widely used because it is a prototypical configuration that can display most of the relevant granular flow phenomena such as avalanching and segregation [19, 20]. Processes such as blending and mixing, and grinding of some materials such as cement, fertilizer, chemicals and pharmaceuticals are commonly carried out in rotating cylinders [21]. In the chemical and process industries, rotating drums are extensively used as mixers, dryers, granulators and reactors for processing granular materials [22].

2.3 Dynamic angle of repose and friction

If we tilted a box of granular material, the material will not start flowing unless a certain angle at the surface is exceeded. This angle—usually called the maximum angle of stability—depends on the frictional properties and the packing of the granular matter [23]. The angle of repose is the slope which the granular material makes at steady state operation. Knowing the angle of repose may help in designing granular equipment such as silos and hoppers. The angle of repose is one of the basic parameters that governs the segregation of granular materials. The surface flow model—the model developed in this project—is highly connected to the repose angle. This model describes axial segregation in rotating drums as a diffusion process with a negative diffusion coefficient. Then, as presented by Savage [24], the negative diffusion works if the drift due to differences in angles of repose exceeds the effect of the Fickian diffusive flux. The other competing mechanism for axial segregation in rotating drums, presented by Aranson et al. [12], is based on traveling wave transience. A key factor in this model is the dynamic angle of repose. We note this innovation here and interpret the dynamic angle of repose as accounting for the friction at the bottom of the flowing layer (commonly referred to as the toe in the engineering literature) which is different from that at the top of the flowing layer (commonly referred to as the shoulder in the engineering literature) where the bed is instantaneously at rest.
In dense granular flows, particles undergo both collisions and frictional (contact) interactions with neighboring particles [25], with the latter playing an important role in flow dynamics and flow trajectory. In this project, we have modeled the flow of particles in rotating drums with three kinds of frictional properties:

1. Average or bulk friction (μ),
2. inter-particle friction μ_i, and
3. friction between particles and drum walls (μ_w).

2.4 Segregation of granular materials

One of the striking properties of granular materials that is composed of different species, is their ability to segregate into their constituent species upon flow or

external vibration. The particles preferentially collect in one or another physical zone of a collective [26]. Due to the fundamental interest as well as its role in granular material industry, segregation of granular media has received a great deal of attention and significant effort has been invested in understanding this puzzling phenomenon [27]. It is well-known that segregation can reduce the quality of final products and affect the efficiency of processes by slowing down the production, which leads to profound economic consequences. Particulate segregation can occur in different devices and configurations, such as rotating drums (this will be presented and discussed in more detail in Chapter 4), hoppers and chutes.

2.5 Segregation mechanisms

In order to obtain segregation in granular mixtures, sufficient differences in one of the particle's properties (size, density, shape, surface roughness etc.) must be achieved. De Silva et al. [26] classified particle segregation into thirteen mechanisms, namely:

1. "Percolation: smaller particles fall through void spaces between larger particles, sometimes as a result of localized shear.
2. Trajectory: caused by a greater speed reduction for smaller particles due to air drag.
3. Air current: fine particles are deposited at silo walls by air currents created by falling particles.
4. Rolling: large or rounded particles roll down the surface of a particle heap in formation.
5. Sieving: smaller particles flow downward through a sliding or rolling layer of larger particles.
6. Impact: a segregation mechanism where more bouncy particles are found further away from the center of a heap in formation.
7. Embedding: larger or denser particles penetrate the surface layer of a heap and become locked in position there.

8. Angle of repose: components with lower angle of repose flow more easily toward the edges of a heap.

9. Push-away: lighter particles are pushed towards the edge of a heap by equally sized heavier particles falling on the apex of the heap.

10. Displacement: larger particles rise above smaller particles as a result of vibrations.

11. Fluidization: fine or lighter particles are kept fluidized at the surface of the particle mixture.

12. Agglomeration: very fine particles form larger aggregates with greater mobility.

13. Concentration driven displacement: occurs in rotating devices where fine particles concentrate in zones due to higher mobility"

These thirteen segregation mechanisms were reduced into four main methods by Johanson [28] and Carson et al. [29]. The reduction comes from considering some of these mechanisms as subsets of others since they occur infrequently [30].
In this section we present two of these fundamental mechanisms that are widely used to explain and predict the segregation process: sifting, which is the basic mechanism, and angle of repose segregation, which is more connected to axial segregation in rotating drums.

- Sifting: Sifting (Fig. 2.2) is caused when fine particles pass through the inter-particle pore structure of the material during shear or vibration [31]. However, in order to obtain sifting segregation, particles must have significant diameter (size) variation, which is usually three (or more) times the mean diameter. Sifting, also known as percolation, is probably the best understood segregation mechanism [32].

  The following factors affect and govern the rate of the sifting process [31]:

  1. The size of the fine particles.
  2. The degree to which the pore structure is already filled.
  3. The amount of cohesion of the fines.

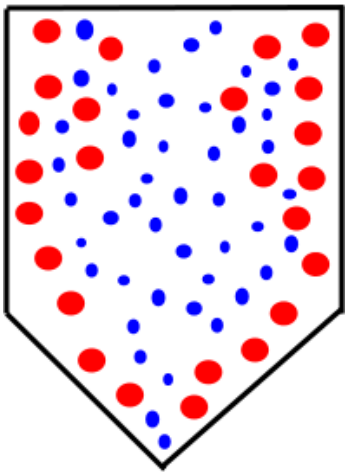

FIGURE 2.2: Fine (blue) particles pass through coarse (red) particles causing sifting segregation.

4. The degree of exposure to new pore structures during movement.
5. The rate of shear.
6. Induced external forces.

Sifting segregation often occurs during handling of granular particles.

- Angle of Repose:
  Angle of repose segregation occurs when two (or more) components of the material mixture have different frictional characteristics [31]. Differences in inter-particle friction lead to the formation of piles with different repose angles. Formation of piles within process equipment causes the less frictional particle to slide further down the pile and accumulate at the pile's edge [33]. Particles with a smaller angle of repose flow over particles with a larger angle of repose. [30]. A two degree difference in repose angle between mixture components is enough to cause significant segregation [31]. Segregation by the angle-of-repose mechanism often magnifies a size segregation because fines usually have a higher angle of repose than coarse particles of the same material [34].

2.6 Axial segregation of granular materials

Axial segregation (Fig. 2.3) is the segregation of binary granular mixtures into alternating bands (streaks) along the rotation axis in a horizontal, partially filled

rotating drum. However, the constituents of the mixture, instead of mixing, tend to segregate from each other, forming bands along the drum axis.

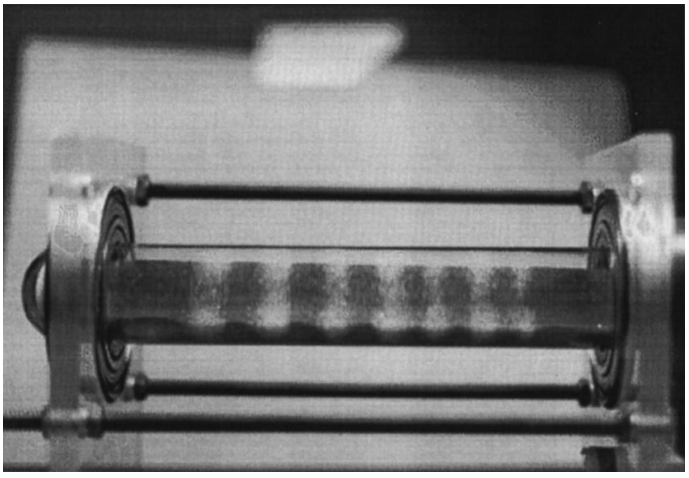

FIGURE 2.3: Axial segregation in a horizontal, partially filled rotating drum. Different bands appear along the drum axis after short period of rotation [11].

This complex phenomenon, which is described several times in the literature [35–39] was first observed by Oyama in 1930 [40] who used bi-disperse mixtures of limestone particles. Donald and Roseman [41] then followed on with a systematic scientific picture in 1962. Using binary mixtures of sand, salt and glass beads, they reported that no bands would form in the central part of the mixture if the angle of repose of the smaller particles was smaller than that of the larger particles. A few theoretical models [7, 24, 42] and several experiments [7, 43–46] have since emerged to better understand band formation and its evolution with time. Besides the development of theoretical models and experimental studies, computational simulation tools like the Discrete Element Method (DEM) [47–50] have also grown rapidly with improvements in computing power. Unfortunately, the time scales of axial segregation are still outside the capabilities of desktop computers, requiring super-computing capabilities to produce meaningful results.

Experimental studies of axial segregation have taken into account the variation of the mechanical properties (size, shape, density and surface roughness) in mixtures of binary, ternary and more components of granular particles. For example, Newey et al. [46] studied axial segregation of granular materials in multi-component mixtures (by size) and observed an array of bands within bands along the length of the drum for ternary mixtures, Fig. 2.4. They also reported that bands in ternary mixtures appeared to oscillate axially under some conditions, while in mixtures of more than four particle sizes, axial segregation was not observed. We

note that the larger particles constitute the darker bands while the smaller ones are identified by the lighter bands.

On the theoretical side, a few segregation mechanisms have been presented based on the free-surface shape [7, 11], dynamics of the repose angle [12] and sub-diffusive axial transport of granular materials [51].

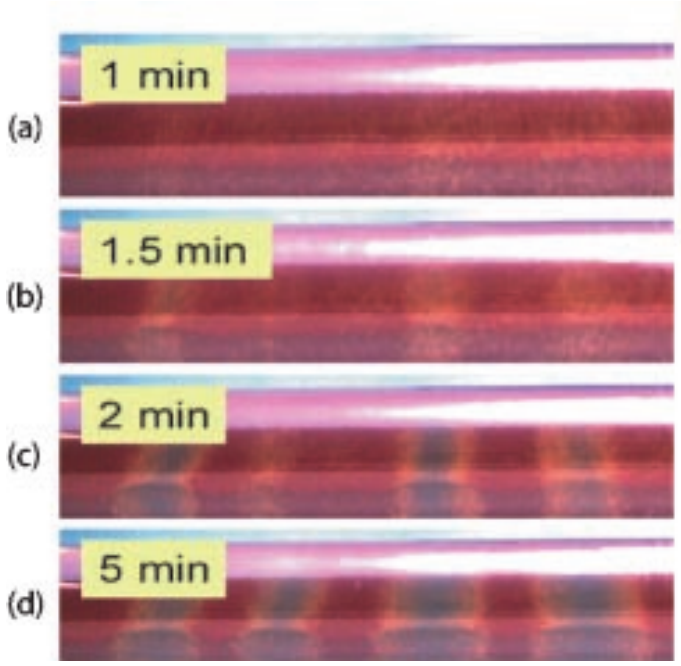

FIGURE 2.4: The medium-sized particles first form surface bands within the largest particles (1.5 min) and the smallest particles then form bands within the medium-particle bands (2 min) [46].

It is not necessary that the shape of the drum be cylindrical, as axial segregation has been observed in drums with square cross-sections, as shown in Fig. 2.5 by Hill et al. [52].

2.7 Coarsening effect

The hallmark of the axial segregation process, is the coarsening effect which occurs with long time evolution. Some bands combine together forming wider bands, some bands shrink or ultimately vanish and some bands grow with time. This fascinating phenomenon has been observed experimentally and studied theoretically. Meier et al. [53] concluded that coarsening seems to be driven by transport of small (or dense) particles from band to band through the semicircular radial core. Frette

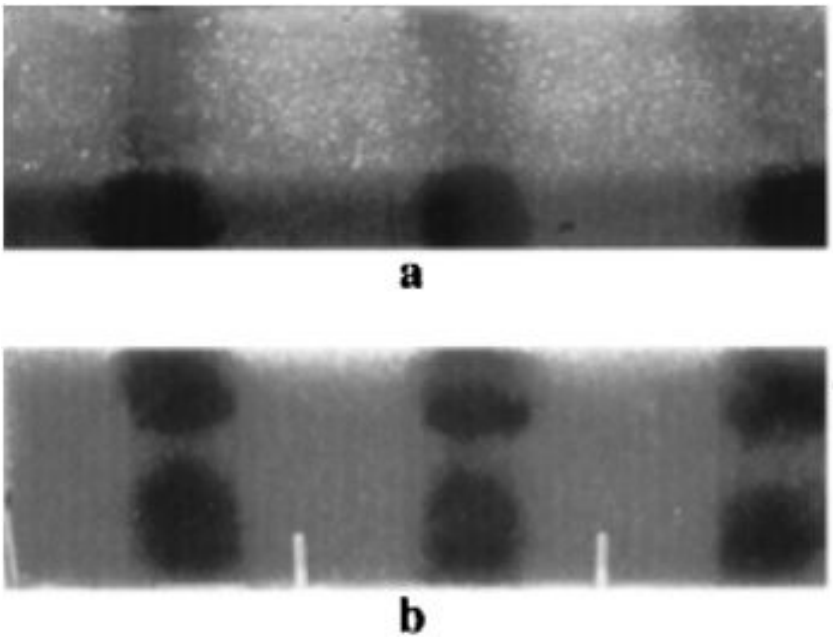

FIGURE 2.5: Axial segregation of a binary granular mixture in a square cross-section drum: (a) in the flowing layer and (b) on side view of the mixer [52].

and Stavans [54] experimentally showed that some bands form and remain stable for almost the entire duration of the experimental run, while others cannibalize one or more smaller bands and persist for the remainder of the experiment. As will be presented in Chapter 4 and Section A.4, one of the main objectives of this project is to reproduce the subsequent coarsening, by suitable extensions of the surface flow model.

Chapter 3

Free Surface Modelling and PEPT Experiments

3.1 Introduction

The purpose of this chapter is to formulate and calibrate models of the free surface for subsequent use in the axial segregation modelling and simulation described in Chapters (4 & 5) respectively. Two models are considered: The Newtonian formulation according to [7] and the Bagnoldian approach [55]. In both cases we obtain explicit forms of the differential equations. To incorporate drum length into the formulation we incorporate the linear scaling law according to [56]. An additional boundary condition based on the estimated filling fraction spanned by the dynamic granular media is introduced for simultaneous solution with the free surface differential equations. To understand the range of validity of the large parameter set constituting the model, Positron Emission Particle Tracking (PEPT) measurements are obtained of a tumbling mill operated in the cataracting Froude regime. The measured free surface profile is employed in an iterative least squares solution scheme with the model-predicted surfaces to obtain an optimised parameter set that serves as the basis for the parametric study of the free surface models. The parametric study is not exhaustive, but rather focuses on identifying those parameter sets that lead to axial diffusion for drum fillings $< 50\%$.

The next two sections describe the PEPT methodology, experimental program and related data analysis performed in this thesis. Sections (3.4 & 3.5) describe the

model development and related boundary conditions for solving the differential equations. The key ingredient to axial segregation for drum fillings less than 50% is routed in the asymmetry of the free surface profile: Section (3.6) illustrates the asymmetry along with the optimised parameter set. The chapter is concluded with a parametric study of the various Newtonian and Bagnoldian parameters.

3.2 Positron Emission Particle Tracking (PEPT)

Positron Emission Particle Tracking (PEPT) is a non-invasive 3D imaging technique that tracks the motion of a representative grain (the tracer) that has been radio-labelled with a positron emitting radionuclide and allowed to move within the field of view (FoV) of a modified Positron Emission Tomography (PET) scanner. Decay by β^+ emission is quickly followed by annihilation with an electron, producing a pair of 511 KeV back-to-back gamma rays that define a line of response (LoR) passing through (or very close to) the tracer. A chronological series of coordinate pairs mostly corresponding to the endpoints of the LoRs constitutes the raw data. A selection of LoRs are then triangulated into grain coordinates $(X_p,\ Y_p,\ Z_p,\ t_p)$ [57, 58] and constitute the measured data for studying granular flow. Fig. (3.1a) is a 2D illustration of a few such LoRs while Fig. (3.1b) is actual data obtained over several milliseconds of data sampling. The spurious LoRs are removed using an iterative algorithm resulting in a redundant set of lines (in 3D) whose intersection (in the least squares sense) defines the best estimate of the tracers position during the chosen time interval (usually a few milliseconds); see Fig. (3.1c). Typically, the 3D spatial coordinates of the tracer are accurate to within a millimeter at a temporal resolution of a few milliseconds. The "EXACT3D" (Model: CTI/Siemens 966) PET scanner employed in this work was designed with the aim of achieving high sensitivity and resolution using state-of-the-art detectors, Fig. (3.2). The device consists of 48 rings of standard bismuth germinate detector elements with a usable ring diameter of ≈ 50 cm and an axial FoV of ≈ 23 cm. The I/O and computing hardware can maintain a sustained acquisition rate of up to four million coincidence events per second. The scanner has been used for clinical research at Hammersmith Hospital, London since 1995, and may still be the most sensitive PET scanner in operation today. It is presently housed at the positron imaging facility, PEPT Cape Town, which is located at the South African national accelerator center, iThemba Laboratory for Accelerator

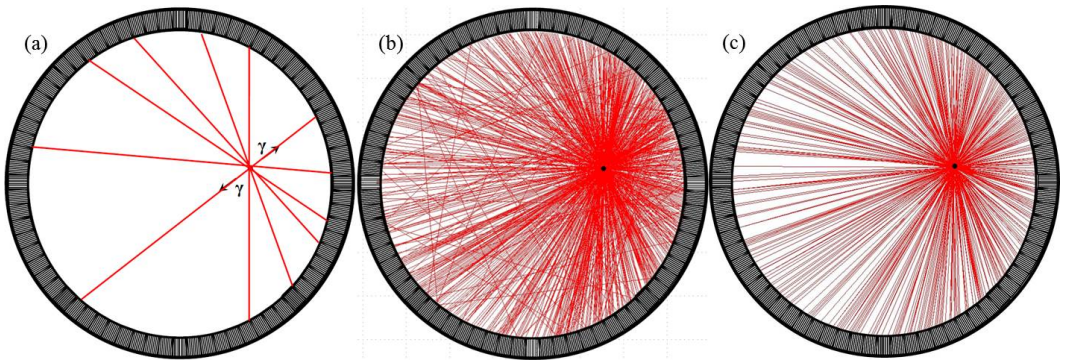

FIGURE 3.1: (a) Illustration of a selection of lines of response (LoRs) emanating from the tracer particle and terminating on the ring of detector elements. (b) A typical set of LoRs sampled over a few milliseconds. (c) The remaining LoRs after the spurious LoRs have been iteratively removed.

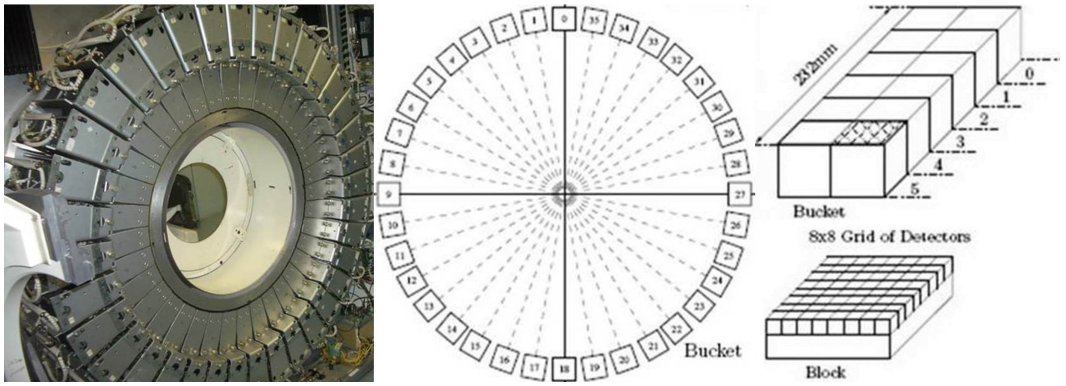

FIGURE 3.2: The "EXACT3D" PET scanner (left) used at PEPT Cape Town with protective cover removed. The 36 detector buckets (middle), each contain 768 Bismuth Germinate detector elements (right) of area (4.8×4.8) mm^2.

Based Science (iThemba LABS). In many PEPT studies the tracer particles are labelled indirectly by attaching a suitable radionuclide to it. In the present study, ^{68}Ga (half-life of 68 minutes) was adsorbed onto a small resin bead ($\sim$ 200 μm) which was then embedded into a representative five millimeter glass bead. Using this method, activities of up to 1.3 mCi was successfully achieved.

3.3 Experimental & data preprocessing

A cylindrical drum with inner diameter of $D = 300$ mm, inner length $W = 285$ mm and wall thickness of 12 mm was built from high density polyethylene (HDPE; specific density 0.95). Fig. (3.3a) shows the rotating drum within the FoV of the PEPT scanner. Twenty, evenly spaced aluminium lifter bars were lined along the inner azimuthal wall, Fig. (3.3b). The two Perspex (circular) end caps present a

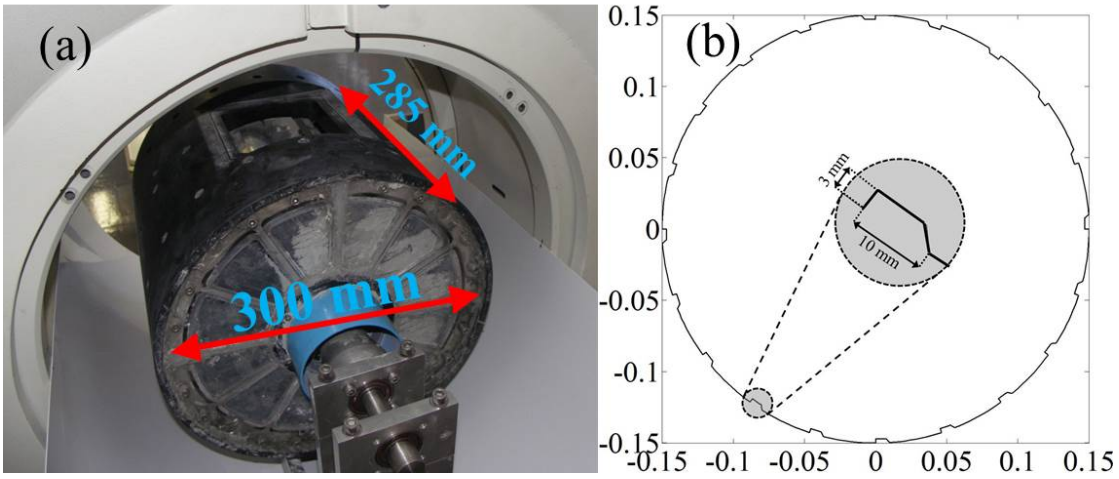

FIGURE 3.3: (a) Experimental rotating drum within the field of view (FoV) of the PEPT camera. (b) Front view schematic of rotating drum showing the twenty aluminium lifter bars. The drum was rotated clockwise to minimise slip by supporting the outer layer of granules.

rough (high friction) surface to the adjacent granular media thereby counteracting excessive slip. The experiment was performed with a 30% filling of mono-sized glass beads having diameter $d = 5.007 \pm 0.025$ mm. A torque sensor coupled directly to the main drive shaft allowed for direct torque measurements with a near-constant torque indicating that steady flow conditions have been reached. A non-contact, optical tachometer was also used to directly monitor the drum rotation speed which further aided in establishing steady state operation. PEPT data logging only commenced once the torque and speed readings were properly stabilised.

The time-averaged velocity (taken component wise) was computed within each of the 100×100 rectangular voxels spanning the flow space. The PEPT velocities were obtained by fitting a 2^{nd} order Lagrange interpolation polynomial to the position-time (X, Y, Z, t) data, interpolating and then differentiating. The resultant azimuthal velocity profile for the drum rotated at 70% of critical speed (54 rpm) is shown in Fig. (3.4a). Using the turning points along the region separating the rising en-masse from the flowing layer to determine the initial location of the equilibrium surface (ES), black squares in Fig. (3.4a), subsequent spline fitting to the initial locations yields the equilibrium surface (dashed-dotted black line) shown in Figs. (3.4a & 3.4b).

Fig. (3.4b) illustrates the corresponding time-averaged volume concentration distribution per voxel $\phi(X, Y)$ according to the implementation by [59] and [60].

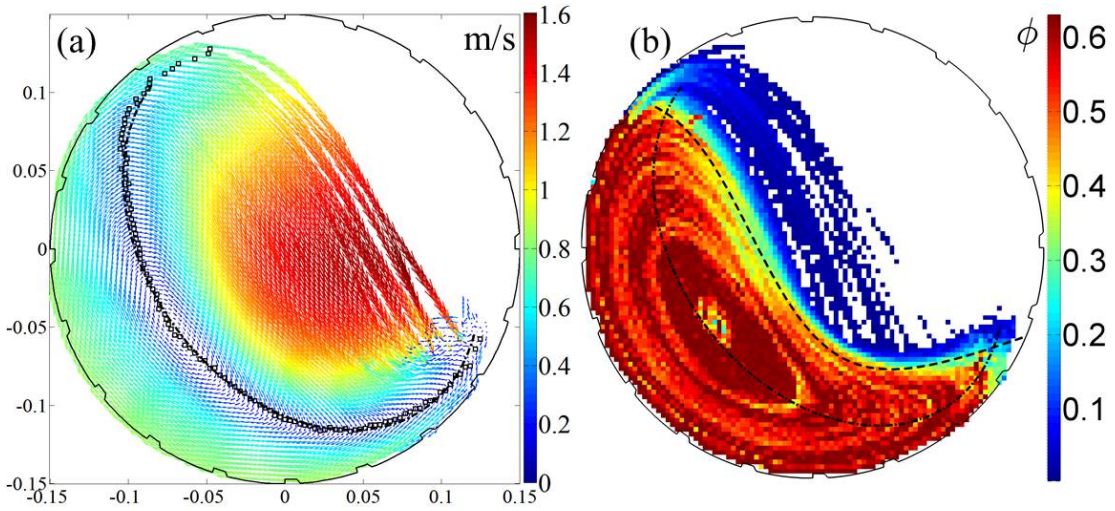

FIGURE 3.4: Time and volume averaged (a) velocity field and (b) volume concentration distribution as determined from typical PEPT analysis of the representative tracer particle (5mm glass bead "labelled" with ^{68}Ga) moving with the mono-sized granular bulk (5mm glass beads occupying 30% of the drum inner volume) in a 300mm diameter tumbling mill operated at 70% of critical speed. (a) Velocity field with equilibrium surface (ES) superimposed. (b) Volume concentration distribution with ES and FS superimposed.

Applying an edge detection scheme [61] to the resulting $\phi(X, Y)$ map allows for the determination of the free surface profile (FS). The black dashed line in Fig. (3.4b) is the free surface profile after a smoothing spline was applied to the edge-detected free surface profile.

3.4 Free surface modelling of rotating drum flows

Beyond rotating drums with rough azimuthal faces (roughness achieved by lining the inner azimuthal wall with granular material) typically studied in the physics literature [7, 55, 62], the case of industrial tumbling mills with lifter bars of varying geometries has only been dealt with empirically in the minerals engineering literature [63–65]. Within the context of industrial boundary conditions the shape of the free surface (excluding the cataracting or in-flight regime) has been approximated only insofar as it facilitated the calculation of power drawn by the flowing material (rock, steel balls and slurry) against the rotation of the drum. Fig. (3.5) shows the two most common free surface shapes employed in the mineral's engineering literature; see [63–65] for more details.

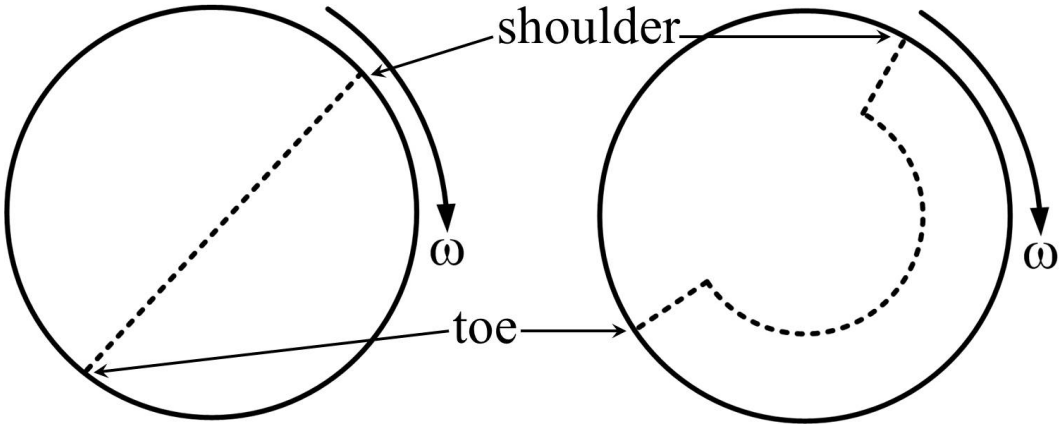

FIGURE 3.5: Illustration of typical free surface shapes (the dashed lines) employed in the mineral's engineering literature. The top and bottom of the free surface are commonly referred to as the shoulder and toe respectively.

For inertially driven granular flow, [13] experimentally showed that the shear stress (δ_{xz}) governing non-Brownian motion varies like $A\left[\frac{\partial v_z(x)}{\partial x}\right]^2$, where $A = \alpha\rho_m\left(\lambda d\right)^2$ such that ρ_m is the material density, d denotes the grain diameter (effective size), $\lambda = \frac{1-\frac{7}{16}\phi}{(1-\frac{\phi}{\phi_c})^2} - 1$ is the linear grain concentration, ρ is the bulk density, $\phi = \frac{\rho}{\rho_m}$ denotes the volume concentration with a critical value of $\phi_c = 0.63$ and α is a dimensionless constant of proportionality which we set to one for numerical convenience.

By assuming a thin, parallel flowing layer of depth x_0 as illustrated in Fig. (3.6), [55] proposed an elementary approach for non-Brownian particles in which he extended Coulomb's balance of stress available for statics to include a dissipation term due to inter-particle collisions. He then argued that the modified Coulomb friction varies like $A\left[\frac{\partial v_z(x)}{\partial x}\right]^2$ because both the momentum lost at each collision and the rate of collision per unit time are proportional to $\frac{\partial v_z(x)}{\partial x}$. Consequently, equality between dissipative stress and motive stress in the steady regime leads to

$$A\left[\frac{\partial v_z(x)}{\partial_x}\right]^2 = \rho g x\left[\sin(\theta) - \mu\cos(\theta)\right] \tag{3.1}$$

where θ is the local repose angle of the flowing layer and $\mu = \tan(\theta_c)$ is the solid friction coefficient according to Coulomb's theory (a material property).

Integrating with suitable boundary conditions then yields an expression for the flowing layer velocity $v_z(x)$:

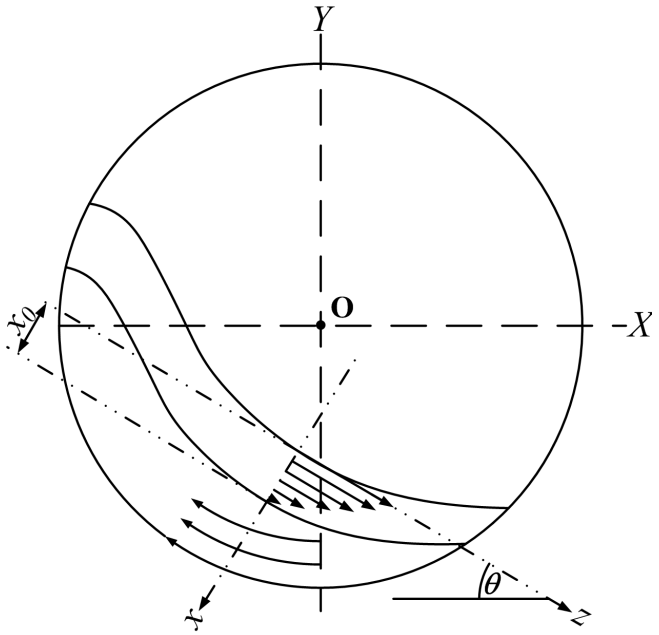

FIGURE 3.6: Illustration of the velocity profile along a perpendicular to the thin (but finite sized) layer of the free surface. The rising en-masse layer below the surface of zero velocity is assumed to move like a solid plug. Note that the Z-axis is out of the page.

$$v_z(x) = \frac{2}{3\sqrt{A}} \left[\cos(\theta)\left(\tan(\theta) - \mu\right)\right]^{1/2} \left[1 - \left(\frac{x}{x_0}\right)^{3/2}\right]. \tag{3.2}$$

The corresponding mass flux per unit length (Φ_f) across the flowing layer is:

$$\begin{aligned} J_f &= \int_0^{x_0} \rho v_z(x) dx \\ &= \frac{2\rho}{5\sqrt{A}} \left[\cos(\theta)\left(\tan(\theta) - \mu\right)\rho g x_0^5\right]^{1/2}. \end{aligned} \tag{3.3}$$

By assuming nearly solid body rotation of the rising region it is easily shown that the corresponding flux reduces to $J_p = \frac{\rho\omega}{2}\left[R^2 - X^2 - Y^2\right]$ after integration, where $R = D/2$ denotes the inner radius of the drum and ω is the drum rotation speed in [rad/s].

At steady state $J_f = J_p$. Substituting $\cos(\theta) = 1/\sqrt{\tan^2(\theta) + 1}$ and noting that $\tan(\theta) = \frac{dY}{dX}$ is the local slope to the free surface in the coordinate system of the drum, the corresponding Bagnoldian free surface—with normalised coordinates ($\widetilde{X} = X/R, \widetilde{Y}_s = Y_s/R$)—is given by equation (3.4):

$$K_B \left[\frac{\frac{\partial \widetilde{Y}_s}{\partial \widetilde{X}} - \mu}{\sqrt{1 + \left(\frac{\partial \widetilde{Y}_s}{\partial \widetilde{X}}\right)^2}} \right]^{0.5} = 1 - \left(\widetilde{X}\right)^2 - \left(\widetilde{Y}\right)^2 \quad \text{with} \tag{3.4}$$

$$K_B = \frac{4\sqrt{(\phi g x_0^5)}}{5\lambda\omega d R^2}. \tag{3.5}$$

Motivated by experimental observations of segregation in a binary mixture of similar sized glass beads and sand, [7] proposed a mechanistic model of the free surface shape and segregation. The flow geometry and coordinate system employed by [7] is similar to Fig. (3.6). By assuming a thin flowing layer of constant depth (x_0) and approximating it to a Newtonian fluid $\left[\delta_{xz} = \eta \frac{\partial v_z(x)}{\partial x}\right]$ with a constant viscosity η, the resulting force balance per unit area between gravity and a Coulomb-like frictional force recovers, after integration, the flowing layer velocity $v_z(x) \propto x^2$. A subsequent flux balance (per unit length of the drum) between the flowing layer and the rising bulk under steady flow conditions then leads to the equation of the free surface.

$$K_N \frac{\frac{\partial \widetilde{Y}_s}{\partial \widetilde{X}} - \mu}{\sqrt{1 + \left(\frac{\partial Y_s}{\partial \widetilde{X}}\right)^2}} = 1 - \left(\widetilde{X}\right)^2 - \left(\widetilde{Y}\right)^2 \quad \text{and} \tag{3.6}$$

$$K_N = \frac{2\phi g \rho_m x_0^3}{3\eta\omega R^2}. \tag{3.7}$$

The extension of the friction mechanism to include sidewall effects (end-caps at axial positions $+W/2$ and $-W/2$ from the centre of the drum, length W) was proposed by [56]. Using a balance of momentum for the flowing layer, an approximate linear scaling law linking the local free surface angle (θ), the depth (x) and the drum length (W) was proposed:

$$\tan(\theta) = \mu_i + \left(\frac{x}{W}\right)\mu_w, \tag{3.8}$$

where μ_i is the inter-particle friction at a depth x below the free surface and μ_w accounts for particle-sidewall interactions. A useful consequence is that at the

bottom of the free surface, i.e. $x = x_0$, $\tan(\theta) = \mu_b$ which relates the shear and normal stresses at the base of the flowing layer. While [56] do propose a model for the free surface, we note that the Newtonian stress ansatz persists in their formulation and thus exclude it from our analysis due to its failure to recover axial banding for drum fillings less than 50%. Notwithstanding, the friction law is an important contribution in that it includes sidewall friction, drum length and bed depth when $\tan(\theta) = \mu_b$.

The present work uses equation (3.8) in combination with the Bagnoldian free surface model, equation (3.4), to successfully recover banding and eventual band coarsening for drum fillings $< 50\%$.

3.5 Boundary conditions

To solve the free surface equations requires initial boundary conditions. When the drum is in steady operation, the granular bed occupies a certain fraction of the drum volume. This dilated filling fraction (α_d) is greater than the static filling (α_s) and is not readily known or easily calculated. It is, however, possible to estimate it in the case of a fully symmetric free surface profile. In particular, for a drum filling of less than half (which is the primary focus of this thesis) we note that the S-shaped free surface profile is an odd function about some inflection point [66]. This implies that the area below the free surface profile is well approximated by the area below straight line $\overline{AB}$; see Fig. (3.7). Noting that the filling fraction for a homogeneous mixture is

$$\alpha_d = \frac{\text{cross–sectional area of bed}}{\text{cross–area of cylinder}}, \tag{3.9}$$

it is easily shown that the area of the bed is given by:

$$\begin{aligned} \text{area of bed} &= \text{area of sector BOA} - \text{area of triangle BOA} && (3.10)\\ &= \frac{1}{2}R^2(2\phi) - 2\left[\frac{1}{2}d(\sin\phi)\right] && (3.11)\\ &= R^2\phi - dRsin\phi, && (3.12) \end{aligned}$$

where $\phi = \widehat{LOB}$ and, hence, the tube filling fraction is given by

$$\alpha_d = \frac{\phi}{\pi} - \frac{1}{\pi R} d \sin \phi. \tag{3.13}$$

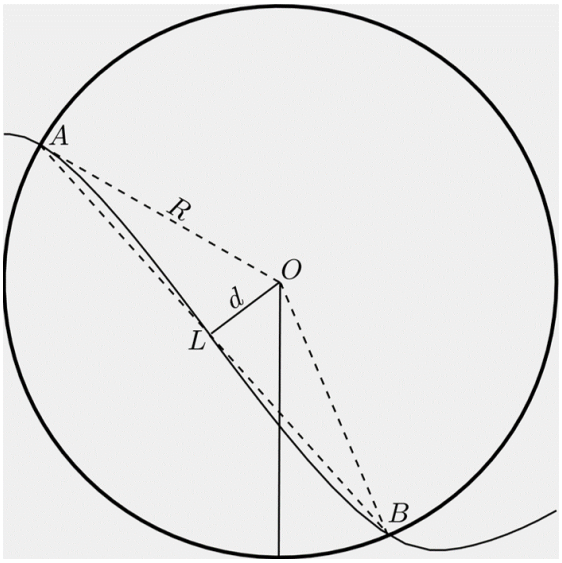

FIGURE 3.7: Illustration of the odd functional form of the symmetric free surface about the inflection point L. The area below line $\overline{AB}$ is equivalent to the area under the free surface profile for a fully symmetric profile. This fact greatly simplifies the estimation of the drum filling fraction.

Equation (3.13) can now be solved simultaneously with equations (3.6 or 3.4) to obtain the free surface profile and corresponding inflection point. We note that equation (3.13) is not exact for surfaces that deviate from symmetry. Accordingly, it is not strictly valid for the Bagnoldian free surface, equation (3.4). Given that the Bagnoldian dilation is strongly dependent on the average friction (μ), the dilation according to equation (3.13) is set as an initial value for the Bagnoldian fitting and allowed to vary with the other fitting parameters in the solution scheme. It is thus expected that certain unrealistic parameter choices can lead to a unrealistic dilation of the bed. To further ensure that our eventual objective—axial segregation for drum fillings less than 50% of drum volume is achieved—we exclude *apriori* those simulations for which the bed dilates to $> 50\%$ of drum volume.

3.6 Asymmetry of Bagnoldian free surface

To illustrate the asymmetry introduced by the Bagnoldian free surface model we consider the rotating drum configuration described in Section (3.3). By fitting (in

the least squares sense) the Bagnoldian (equation 3.4) and Newtonian (equation 3.6) models of the free surface to the measured (via PEPT) data we obtained Fig. (3.8) with the corresponding parameters (known, measured and fitted) given in Table (3.1). The symmetry line in Fig. (3.8)—which is equivalent to straight line $\overline{AB}$ in Fig. (3.7)—is denoted by the straight black line. The Newtonian free surface is shown by the half-red and half-blue line with a magenta dot at the intersection of the red-blue line indicating the inflection point. Accordingly, any profile that is symmetric will also cut the symmetry line at the inflection point. However, on closer inspection of Fig. (3.8) the Bagnoldian free surface profile (green profile)—and indeed the measured (via PEPT) free surface profile (black, dashed profile)—clearly do not pass through the inflection point and is thus asymmetric. The asymmetry implies differences in frictional properties between the upper (green profile) and lower (blue profile) sections of the curve. And given that the upper section (green profile) flows from an instantaneously stationary shoulder while the lower section (blue profile) is fully developed accelerated flow, the expectation is that the friction should be higher (respectively, lower) in the upper (respectively, lower) section. We assert that it is this asymmetry that ultimately drives the initial stages of axial segregation and banding. As will be discussed in Chapter (4), this asymmetry is not sufficient to achieve band coarsening, so further extension of the axial diffusion theory is needed.

Parameter	**Newtonian**	**Bagnoldian**
Grain size (d)	5 mm	5 mm
Density of glass beads (ρ_m)	2500 kg/m^3	2500 kg/m^3
Average friction coefficient (μ)	0.62	0.56
Inter-particle friction coefficient (μ_i)	none	0.44
Wall friction coefficient (μ_w)	none	0.63
Basal friction coefficient (μ_b)	none	0.72
Drum length (W)	0.285 m	0.285
Internal drum radius (R)	0.15 m	0.15 m
Angular speed (ω)	54 rpm	54 rpm
Filling fraction (α_d)	0.4137	0.4137
Solid concentration (ϕ)	0.6	0.6
Linear grain concentration (λ)	none	5.5
Viscosity (η)	5 Pa.s	none
$x_0 = \frac{W(\mu_b - \mu_i)}{\mu_w}$	0.0825 ($\approx 16d$)	0.0483 ($\approx 8d$)

TABLE 3.1: The parameters resulting from the least squares fit of the free surface models to the measured (via PEPT) data of the rotating drum configuration described in Section (3.4).

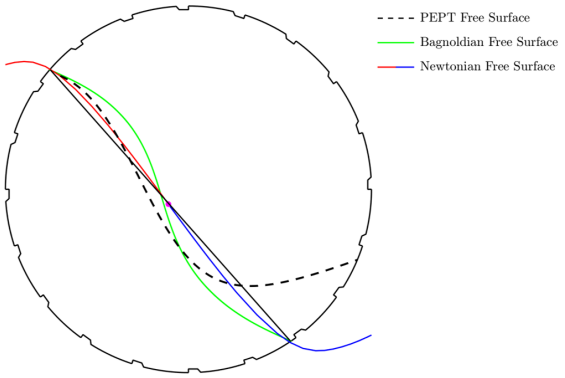

FIGURE 3.8: Illustration of the asymmetric Bagnoldian free surface profile which is argued (in this thesis) to be responsible for the initial stages of axial banding for drum fillings less than 50%.

3.7 Parametric study of free surface models

To illustrate the sensitivity of the free surface models to the various parameters, we conduct a parametric investigation with the parameters in Table (3.1) as our base case.

3.7.1 Effect of viscosity (η) on Newtonian free surface

Starting with the optimised parameter set given in Table (3.1), the viscosity parameter (η) was varied as per Fig. (3.9). The shoulder (respectively, toe) is observed to move upwards (respectively, downwards) with increasing viscosity. The response of the toe and shoulder to changes in viscosity is symmetric as expected. At viscosities consistent with water ($\eta \sim 10^{-3}$), the free surface profile appears flat. The shift towards the characteristics S-shape occurs for relatively high viscosities (~ 1). Given that the viscosity effect only starts to take effect for values that are approximately 1000 times larger than typical fluid viscosities, it is clear that the viscosity parameter is more akin to some sort of bulk flow resistance.

3.7.2 Effect of average friction (μ) on Newtonian free surface

The average friction combines the effects of high and low friction species. For a bimodal mixture of high (μ_h) and low (μ_ℓ) friction species with normalised

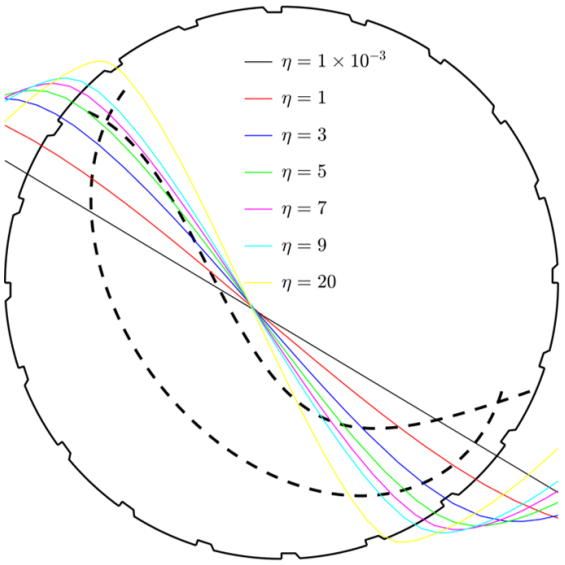

FIGURE 3.9: Influence of viscosity on the Newtonian free surface. All other parameters used for the fit are given in Table (3.1). The upper (respectively, lower) dashed lines refer to the free surface (respectively, equilibrium surface).

concentrations of $\langle C_h \rangle$ and $\langle C_\ell \rangle$ respectively (i.e. concentration varies from zero to one), we define the average friction coefficient as:

$$\mu = \frac{\langle C_\ell \rangle \mu_\ell + \langle C_h \rangle \mu_h}{\langle C_\ell \rangle + \langle C_h \rangle}, \tag{3.14}$$

where $\langle\rangle$ denotes an average quantity.

Starting with the optimised parameter set given in Table (3.1), the friction parameter (μ) was varied as per Fig. (3.10). The shoulder (respectively, toe) is observed to move upwards (respectively, downwards) with increasing friction. The response of the toe and shoulder to changes in friction is inversely symmetric and can be understood in terms of equation (3.14): increasing (respectively, decreasing) the concentration of the high (respectively, low) friction species causes the bed to become more (respectively, less) reposed and consequently the shoulder moves to a higher (respectively, lower) position while the toe moves to a symmetrically lower (respectively, higher) position; and due to symmetry, the opposite is also true.

At viscosities consistent with water ($\eta \sim 10^{-3}$), the free surface profile appears flat while the characteristic S-shape is apparent for all friction coefficients, suggesting a greater sensitivity of the free surface to friction than viscosity.

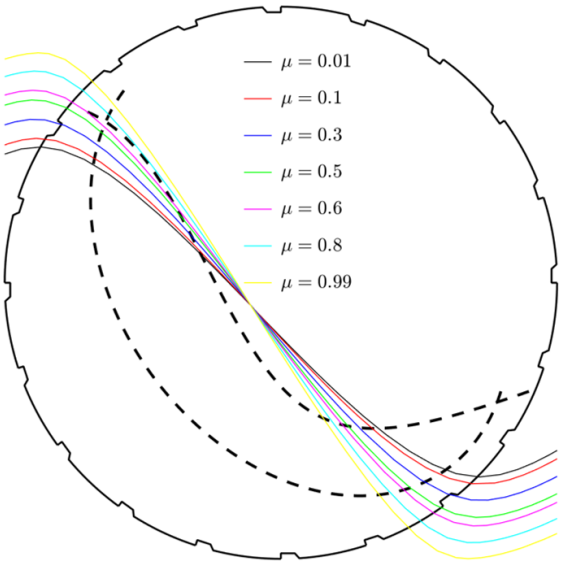

FIGURE 3.10: Influence of friction on the Newtonian free surface. All other parameters used for the fit are are given in Table (3.1).

3.7.3 Effect of average friction (μ) on the Bagnoldian free surface

The influence of the average friction (μ) on the Bagnoldian free surface profile is shown in Fig. (3.11).

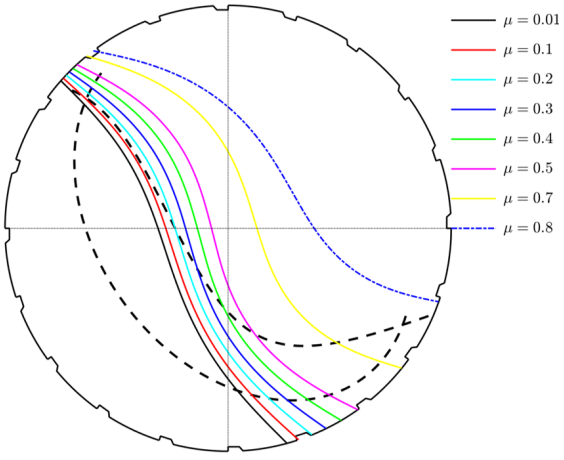

FIGURE 3.11: Influence of average friction (μ) on the Bagnoldian free surface. All other parameters used for the fit are are given in Table (3.1).

The free surface appears to shift systematically upwards with increases in average friction coefficient (μ), resulting in excessive bed dilation for relatively high friction coefficients. The shoulder region appears to be well described by the model; however, the toe region is systematically underestimated, except for relatively high friction coefficients. The underestimation of the toe is partly influenced by

the boundary condition set by equation (3.13): The solution of the differential equation appears to enforce the prescribed filling fraction constraint for $\mu < 0.5$; however, at high values the friction dominates over the loosely-enforced[1] boundary condition. Unfortunately, the friction does not produce a realistic dilation for high friction coefficients ($\mu \gg 0.5$). Various attempts to numerically resolve this issue failed and we thus conclude that only a new formulation of the free surface model can realistically achieve the desired dilation. Fortunately, our objective is to evolve axial segregation for mill fillings less than 50%. Accordingly, we do not consider the axial segregation simulations for $\mu > 0.5$ thus ensuring that our dilated bed occupies less than 50% of the drum volume.

3.7.4 Effect of bed depth (x_0) on the Bagnoldian free surface

The constant bed depth (x_0) employed by the model is clearly a deficiency when compared to the measured (via PEPT) depth. Ideally, a model that accounts for the depth variation is required; however, this was not achieved in the present study. Noting that the bed depth is entirely controlled by the friction law [56] and hence μ_i, μ_w, μ_b and mill length (W), we compare the model-predicted values of x_0 with each other to determine a viable range; see Fig. (3.12): It is clear from the figure that for realistic values ($x_0 > 0$) requires:

1. $\mu_b > 0.44$,
2. $\mu_i < 0.7$, and hence
3. $0.44 < \mu_w < 0.7$.

We note that the optimised parameter set given in Table (3.1) satisfy these conditions.

[1] Attempts to enforce a hard boundary condition causes the solution to fail or produce unrealistic profiles.

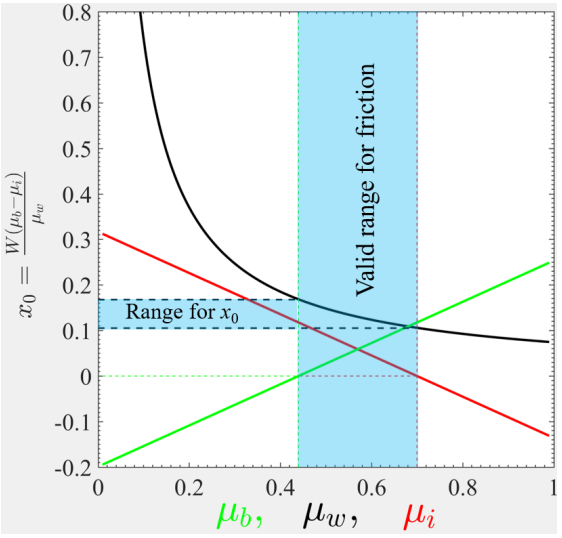

FIGURE 3.12: Variation of bed depth with μ_b, μ_w and μ_i. The cyan colored areas demarcate the valid bed depth range and related range of coefficients (μ_b, μ_w, μ_i and W) for using the Bagnoldian free surface model in combination with the Taberlet's friction law.

3.7.5 Effect of wall friction (μ_w) on the Bagnoldian free surface

Fig. (3.13) illustrates the variation of the free surface with wall friction. The shoulder position remains relatively fixed and well predicted relative to the measured shoulder. Increasing the wall friction causes the toe to shift downwards while simultaneously making the profile more S-shaped. Unfortunately, a reasonable toe prediction for $\mu_w < 0.55$ is offset by a very unrealistic free surface shape and exaggerated bed dilation. Similarly, a reasonable S-shaped profile produces very low toe positions for $\mu_w > 0.6$. It would appear that for the given experimental configuration, as described in Section (3.3), an optimal choice is $\mu_w \approx 0.6$. We note that the least squares fit to the PEPT data confirms this result; see Table (3.1).

3.7.6 Effect of drum speed (ω) on the Bagnoldian free surface

The variation of the free surface with drum rotation rate (ω), in [rad/s], follows a similar trend to the variation with μ_w; see Fig. (3.14) and cf. Fig. (3.13). The mill speed range as a percentage of critical speed (% crit.) is: 20% : 10% : 90%. In mineral processing the rotation rate of the drum is often expressed as a fraction of

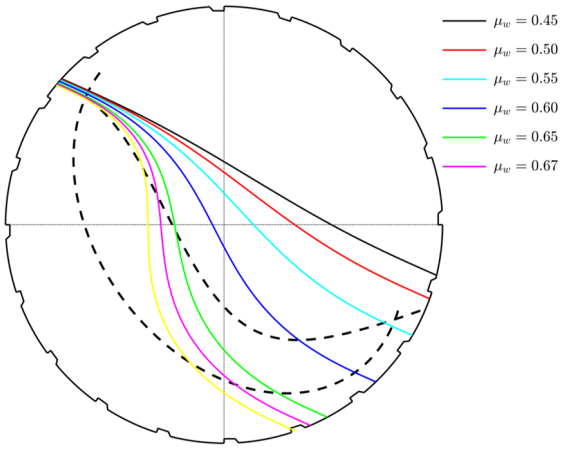

FIGURE 3.13: Influence of wall friction (μ_w) on the Bagnoldian free surface. All other parameters used for the fit are are given in Table (3.1).

the critical speed: The critical speed is the rotational speed at which the outermost layer of granular material begins to centrifuge. It is defined in revolutions per minute (RPM) as:

$$N_c = \frac{1}{2\pi}\sqrt{\frac{2g}{D-d}}, \tag{3.15}$$

where D is the inner diameter of the rotating drum and d is the diameter of the grains. In the limit that $d \ll D$, which is typical in industrial tumbling mills, the critical speed is usually approximated (in RPM) as:

$$N_c \approx \frac{42.3}{\sqrt{D}}. \tag{3.16}$$

For the given experimental configuration an optimal choice is $\omega \approx 5.7$ which is consistent with the actual mill speed.

3.7.7 Effect of volume concentration (ϕ) on Bagnoldian free surface

Fig. (3.15) shows the variation of free surface profile with volume fraction up to a maximum of $\phi = 0.64$. The trend is quite counter-intuitive, as the bed appears to dilate with a tighter packing density. A possible explanation is that the hydrostatic pressure assumption is incorrect for densely granular flows; see [5] who note

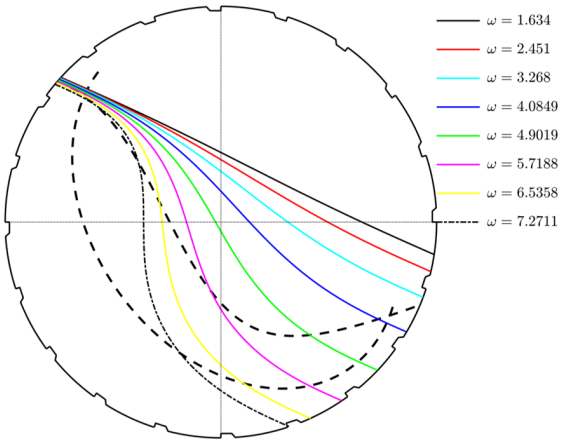

FIGURE 3.14: Influence of mill speed (ω) on the Bagnoldian free surface. All other parameters used for the fit are are given in Table (3.1).

that for an unconfined bed—as is the case for rotating drum flows—the volume fraction is complexly dependent on shear rate, material density and bed pressure. Accordingly, the nonlinearity in pressure can have a corresponding non-linear response in the friction which in turn causes the bed to dilate. Notwithstanding, the result is useful in that it provides an indirect means of testing the influence of material density ρ_m on axial segregation. For the given experimental configuration an optimal choice is $\phi \approx 0.6$ which is consistent with the best fitted value as given in Table (3.1).

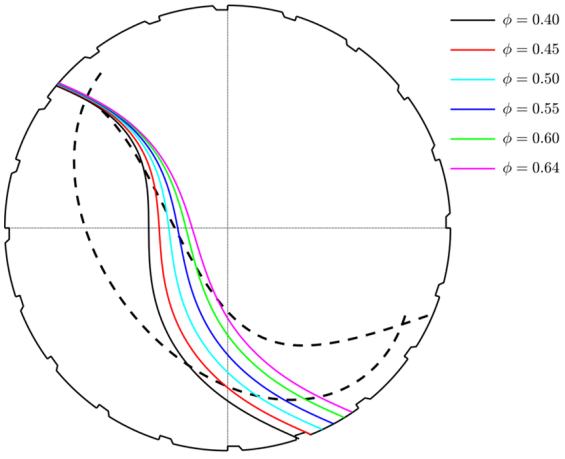

FIGURE 3.15: Influence of volume fraction (ϕ) on the Bagnoldian free surface. All other parameters used for the fit are are given in Table (3.1).

3.8 Summary

A PEPT derived free surface profile of a tumbling mill operated in the cataracting Froude regime was used to obtained (in the least squares sense) an optimised parameter set for fitting Newtonian and Bagnoldian free surface profiles; see Table (3.1). Unlike the Newtonian free surface model, the Bagnoldian result was shown to be asymmetric about the S-shaped inflection point—a key requirement to successfully recovering axial segregation and the related phenomenon of axial banding. A parametric study around the optimised parameter set revealed that:

1. The Newtonian free surface varies symmetrically with viscosity albeit that the effects on the free surface shape is only achieved at very high values ($\eta \sim 1$).

2. The Newtonian free surface varies symmetrically with average friction coefficient with the corresponding shape exhibiting sensitivity across the full range of friction coefficients.

3. The Bagnoldian free surface produces larger variations in the toe than the shoulder in response to changes in average friction, with bed dilation becoming excessive (and unrealistic) for relatively high friction coefficients. With regard to representative profiles for drum fillings less than 50%, $\mu \in [0.1;\ 0.5]$ exhibit reasonable agreement with the PEPT-derived profile.

4. The bed depth range consistent with the thin layer approximation is satisfied for $0.44 < \mu_w < 0.7$.

5. The Bagnoldian free surface becomes more S-shaped with increases in μ_w, but at the expense of a poorly predicted toe. Conversely, the toe prediction improves for lower values of μ_w, but at the expense of a poorly predicted S-shape and an excessively dilated bed. An optimal choice for the current experimental configuration is $\mu_w \in [0.55;\ 0.65]$.

6. The influence of mill speed on the free surface profile is very similar to the influence of μ_w.

7. The free surface profile tends to dilate in response to increases in volume fraction. This appears counter-intuitive; however, deviations from simple hydrostatic pressure could offer an explanation in that it impacts non-linearly on the friction which is known to cause bed dilation.

8. The least squares fitted parameter set lies within the optimal parameter ranges identified through the parametric study.

Chapter 4

Axial Segregation Modelling

4.1 Introduction

Axial segregation in a horizontally rotated drum is the separation of a granular mixture (binary, ternary, etc) into alternating bands (streaks) along the rotation axis. However, the constituents of the mixture instead of mixing, tend to segregate from each other forming bands along the drum axis. The bands form after several hundred drum rotations. As argued in the hypothesis formulation of Section (1.3) the segregation process is based on differences in particle mechanical properties (size, surface roughness, shape, density) which we have heuristically argued to manifest as differences in friction.

Before proceeding further, we introduce a few notational changes in the interest of clearer and more aesthetically pleasing equations:

1. h denotes the flowing layer depth.
2. The global coordinate system is denoted as (x, y, z). In particular, this means that the axial direction is the $z-$direction.
3. Lower case subscripts ℓ and h are used to denote "low" and "high" values respectively.
4. The total flux will be denoted by J and for individual species j_{mz} denotes the flux of the $m^{\text{th}}-$species in the $z-$direction.

The next section elucidates the mechanism governing axial segregation as gravity driven flow with friction-limited mobility that manifests in the form of a diffusion equation, the details of which are given in Appendix (A). Section (4.3) develops the diffusion equation for multiple species: three-, four- and $n-$species. Section (4.4) presents a model for the determining $\frac{dy}{dC}$. Initial concentration profiles consistent with tumbling mills are considered in Section (4.5). The chapter is then concluded with a brief summary.

4.2 Mechanism governing axial segregation

Consider a bimodal mixture of high (μ_h) and low (μ_ℓ) friction species due to, say, size differences. As discussed in Section (3.7.2), the corresponding average friction coefficient is given by equation (3.14) and restated here for convenience:

$$\mu = \frac{\langle C_\ell \rangle \mu_\ell + \langle C_h \rangle \mu_h}{\langle C_\ell \rangle + \langle C_h \rangle}. \tag{4.1}$$

Now consider two adjacent axial slices consisting of the bimodal granular mixture within a 300 mm diameter rotating drum operated at $\omega = 5.7188$ RPM, such that one slice (call it slice 1) is rich in high friction species ($\langle C_{h,1} \rangle = 0.8$; $\langle C_{\ell,1} \rangle = 0.2$) while the other (slice 2) contains an equal mix ($\langle C_{h,2} \rangle = 0.5$; $\langle C_{\ell,2} \rangle = 0.5$). Clearly, slice 1 is richer in high friction species than slice 2. The corresponding free surface profiles of these adjacent slices are shown in Fig. (4.1).

It is also clear from Fig. (4.1) that the mixture dominated by high friction species depicts a higher free surface profile (green) than the equal mixture (magenta). Noting that these are adjacent layers, it is easy to imagine a natural slope forming between them—this slope is the geometric source of axial flow that is driven by gravity. We note that the same is not true for the Newtonian free surface response to average friction (see Fig. 3.10): For adjacent slices of different frictional properties, the upper section (above the inflection point) has an axial gravity slope directed from high-to-low friction surfaces while the lower section (below the inflection point) has the axial gravity slope in the opposite direction. The interplay of these two competing flows will tend to counteract axial diffusion, and is arguably the main reason that it fails to recover axial banding. It is thus surprising that axial segregation occurs even for the drum fillings greater than 50%. Given

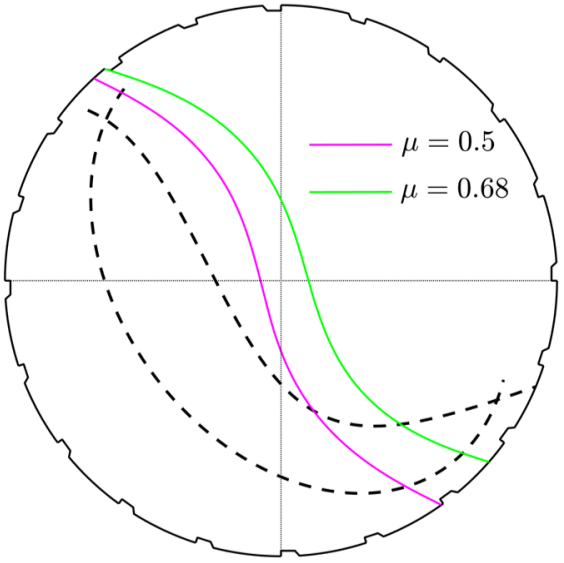

FIGURE 4.1: Bagnoldian free surface profiles for equal (magenta) and unequal (green) concentrations of high and low friction species respectively. All other parameters used for the fit are are given in Table (3.1).

that friction-limited mobility is also at play, it would seem that for the Newtonian formulation to produce axial segregation, the difference in frictional properties of adjacent layers must be significant, cf. [11] who note that even for drum fillings greater than 50%, no axial segregation is observed if the differences in particle size of a bimodal mixture is small.

Noting that experimental observation confirms the existence of axial segregation at drum filling $> 50\%$ and $< 50\%$, the Bagnoldian picture of adjacent free surface profiles of different frictional properties seems more consistent with reality. So provided that the abovementioned mixtures lie side by side, there will exist a slope down which gravity can drive particles. Fig. (4.2) is a schematic (not to scale) of such adjacent slopes formed from different mixtures of friction species.

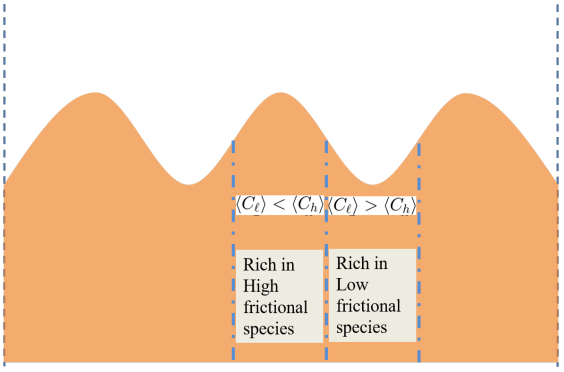

FIGURE 4.2: Adjacent axial slices in a rotating drum with different concentrations of friction species.

Due to material conservation the axial flux down the free surface slope (J_f) is balanced by the back flux (J_b) as illustrated in Fig. (4.3). Applying the flux balance to the constituents of high flux (J_{fh}) and low flux ($J_{f\ell}$), which correspond respectively to the high and low friction species, then yields:

$$\begin{aligned} J_f &= J_b; && (4.2)\\ \Rightarrow J_{fh} + J_{f\ell} &= (n_\ell + n_h)\, h v_z, && (4.3) \end{aligned}$$

where ($n_\ell + n_h = constant$) denotes the number conservation between the adjacent layers comprising of high (n_h) and low (n_ℓ) number of particles and v_z is the velocity in the axial direction, i.e. $z-$direction. The flux terms ($J_{fh},\ J_{f\ell}$) are now also in the axial direction such that the local free surface slope is directed locally in both the $x-$ and $z-$directions.

In terms of number density and the multi-directional gradients the total Newtonian flux becomes (see Appendix A.1 for details)

$$\begin{aligned} J_N &= An\left[1 + |\bigtriangledown_y|^2\right]\left[|\bigtriangledown_y| - \mu\right]\hat{|\bigtriangledown_y}\ ; && (4.4)\\ \Rightarrow J_N &\propto \left[|\bigtriangledown_y| - \mu\right], && (4.5) \end{aligned}$$

where n is the number density of the granular materials, $\hat{\bigtriangledown}_y$ is the unit vector in the $x-$ and $z-$ directions such that $\bigtriangledown y(x,z) \equiv \bigtriangledown_y$ and the constant $A = \left(\frac{1}{3\eta}\frac{P_0^3}{(\rho g)^2}\right)$. Similarly, the total Bagnoldian flux reduces to

$$\begin{aligned} J_B &= \frac{nB\left(|\bigtriangledown_y| - \mu\right)^{1/2}}{\left[|\bigtriangledown_y|^2 + 1\right]^{1/4}}\hat{\bigtriangledown}_y, && (4.6)\\ B &= \frac{2}{5\sqrt{A}}\left[\rho g h^5\right]^{\frac{1}{2}}; && (4.7)\\ \Rightarrow J_B &\propto \left[|\bigtriangledown_y| - \mu\right]^{1/2}. && (4.8) \end{aligned}$$

But the flux terms are clearly proportional to the average friction, and since $\mu_{fh} > \mu_{f\ell}$, this implies that $J_{fh} < J_{f\ell}$ in both the Newtonian and Bagnoldian

formulations. The difference in flux along the free surface layer between high and low friction species sets up a flux differential between J_f and J_b that ultimately manifests as a diffusion instability that we argue as the mechanism for axial segregation. Consequently, as time evolves low friction particles move more freely and accumulate in the lower axial free surface slice; more so than the high friction species. The result is that the concentration of low friction species in the lower slice starts increasing faster than the concentration of high friction species in the lower slice, i.e. the difference in concentration of low friction species (and high friction species) between the adjacent slices starts to become larger with time and hence the difference in frictional properties starts to increase. Consequently a positive feedback of the diffusion flux is achieved that reinforces the depletion (respectively supply) of low friction particles from (respectively to) the left region (respectively right region) as shown in Fig. (4.3). So in the axial (z) direction, gravity drives free surface particles down the slope and friction dictates their mobility.

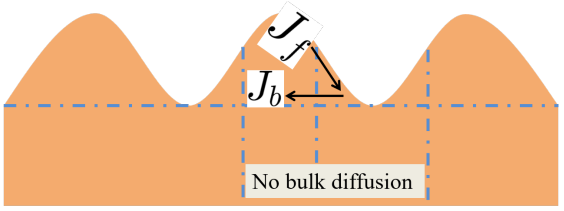

FIGURE 4.3: Illustration of the balance between the free surface layer flux and the back flux.

To maintain a readable exposition in what follows, the bulk of the mathematical details are deferred to Appendix (A) with only the key equations and descriptions provided herein.

Mathematically we write the new gradient at each point along the free surface as:

$$\vec{\nabla}_y = \frac{\partial y}{\partial x}\hat{x} + \frac{\partial y}{\partial z}\hat{z} = y_x\hat{x} + y_z\hat{z}, \tag{4.9}$$

where $y = y(x, z)$. Applying continuity arguments along the axial direction, it can be shown (see Appendix A.3) that the concentration evolution with time is

$$\frac{\partial C}{\partial t} = +\frac{1}{n_0}\frac{\partial}{\partial z}\int_{surface} An_0C(1-C)\left[1+\nabla_y^2\right]\left[\mu_h - \mu_\ell\right].\hat{\nabla}_y. \tag{4.10}$$

Expanding ∇_y^2 to second order (see Appendix A)—which is beyond the original first order approximation used by [7, 11]—then yields after linearisation:

$$\frac{\partial C}{\partial t} = A\left[\mu_h - \mu_\ell\right]\left[\int_{surface}\left[1 + y_x^2 + y_z^2 + \frac{y_z^4}{4y_x^2}\right]\frac{1}{\left[1+\frac{y_z^2}{2y_x^2}\right]}\left(\frac{y_C}{y_x}\right)\right]\frac{\partial}{\partial z}\left[C(1-C)\frac{\partial C}{\partial z}\right], \tag{4.11}$$

where $D = A\left[\mu_h - \mu_\ell\right]\left[\int_{surface}\left[1 + y_x^2 + y_z^2 + \frac{y_z^4}{4y_x^2}\right]\frac{1}{\left[1+\frac{y_z^2}{2y_x^2}\right]}\left(\frac{y_C}{y_x}\right)\right]$ represents a diffusion coefficient such that the final axial segregation model resembles a non-linear diffusion equation for relative concentrations along the axial direction of the drum. In compact form, the familiar diffusion-like equation is given as:

$$\frac{\partial C}{\partial t} = D\frac{\partial}{\partial z}\left[C(1-C)\frac{\partial C}{\partial z}\right]. \tag{4.12}$$

A few important features of the new derivation are worth noting:

1. The use of a Bagnoldian free surface ensures an asymmetric surface profile.
2. Unlike the Newtonian free surface response to increases in average friction (μ) where the upper section is shifted upwards while the lower section is shifted symmetrically downwards, the Bagnoldian free surface is systematically shifted upwards. This ensures that adjacent axial slices with different average frictional properties have a unidirectional slope from the high friction surface to the lower one—this fact ensures unidirectional axial flow between adjacent slices for any drum filling.
3. The expansion of $\bigtriangledown_y^2$ to second order in y_z.

A direct consequence of these new features ensures that the banding and eventual coarsening (see next two chapters) is successfully recovered in the long time evolution.

4.3 Multi-Species Mixtures

Axial segregation of multi-species mixtures have been observed in a few experiments and DEM simulations. The pattern of the bands depends on the number of

species used in the mixture. For example, in the case of a three species mixture, bands within bands are observed as sketched in Fig. 4.4 below.

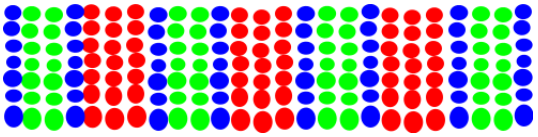

FIGURE 4.4: Bands within bands pattern associated with three species mixture. The three different colors refer to the three different-friction species.

4.3.1 Three Species Mixture

To derive the set of diffusion equations that represent axial segregation of a three-species mixture, using the surface flow mechanism, we follow the same argument that was applied for binary mixtures (described in detail in Section A.1).

First, application of the continuity equation that exists for each species results in:

$$\frac{\partial}{\partial t}C_1 = -\frac{\partial}{\partial z}\int_{surface}\left[\frac{j_{1z}}{n_0} + \frac{n_1 h v_z}{n_o}\right].\widehat{\nabla}_y, \tag{4.13}$$

$$\frac{\partial}{\partial t}C_2 = -\frac{\partial}{\partial z}\int_{surface}\left[\frac{j_{2z}}{n_0} + \frac{n_2 h v_z}{n_o}\right].\widehat{\nabla}_y, \text{ and} \tag{4.14}$$

$$\frac{\partial}{\partial t}C_3 = -\frac{\partial}{\partial z}\int_{surface}\left[\frac{j_{3z}}{n_0} + \frac{n_3 h v_z}{n_o}\right].\widehat{\nabla}_y; \tag{4.15}$$

where C_1, C_2 and C_3 are the concentrations of each of the three species with coefficients of friction μ_1, μ_2 and μ_3 respectively. n_o is the total number density of the particles in the mixture. j_{1z}, j_{2z} and j_{3z} are the (axial) fluxes (per unit length) in the free surface layer given by Eq. 4.19, Eq. 4.20 and Eq. 4.21 respectively. The terms $\left(\frac{n_1 h v_z}{n_o}, \frac{n_2 h v_z}{n_o}, \frac{n_3 h v_z}{n_o}\right)$ are the back flow fluxes.
At any given axial slice:

$$\frac{n_1}{n_o} + \frac{n_2}{n_o} + \frac{n_3}{n_o} = 1 \Longrightarrow \frac{n_1}{n_0} = C_1,\ \frac{n_2}{n_0} = C_2 \text{ and } \frac{n_3}{n_0} = C_3.$$

Addition of Eq. 4.13, Eq. 4.14 and Eq. 4.15 produces:

$$0 = -\frac{j_1 + j_2 + j_3}{n_o} - h v_z \Longrightarrow h v_z = -\frac{j_1 + j_2 + j_3}{n_o}. \tag{4.16}$$

Substituting hv_z into Eq. 4.13 and Eq. 4.14 yields:

$$\frac{\partial}{\partial t}C_1 = -\frac{1}{n_o}\frac{\partial}{\partial z}\int_{surface}\left[(1-C_1)\,j_1 - C_1\,(j_2+j_3)\right].\widehat{\nabla}_y \tag{4.17}$$

$$\frac{\partial}{\partial t}C_2 = -\frac{1}{n_o}\frac{\partial}{\partial z}\int_{surface}\left[(1-C_2)\,j_2 - C_2\,(j_1+j_3)\right].\widehat{\nabla}_y \tag{4.18}$$

The details of axial fluxes ($J_1,\ J_2,\ J_3$) in the free surface layer can be expressed as:

$$\begin{aligned} J_1 &= -\frac{n_1}{3\eta}\frac{P_0^3}{(\rho g)^2}\left[1+|\bigtriangledown_y|^2\right]\left[|\bigtriangledown_y|-\mu_1\right].\widehat{\nabla}_y \\ &= -\frac{n_oC_1}{3\eta}\frac{P_0^3}{(\rho g)^2}\left[1+|\bigtriangledown_y|^2\right]\left[|\bigtriangledown_y|-\mu_1\right].\widehat{\nabla}_y \\ &= -n_oC_1A\left[1+|\bigtriangledown_y|^2\right]\left[|\bigtriangledown_y|-\mu_1\right].\widehat{\nabla}_y \end{aligned} \tag{4.19}$$

$$\begin{aligned} J_2 &= -\frac{n_2}{3\eta}\frac{P_0^3}{(\rho g)^2}\left[1+|\bigtriangledown_y|^2\right]\left[|\bigtriangledown_y|-\mu_2\right].\widehat{\nabla}_y \\ &= -\frac{n_oC_2}{3\eta}\frac{P_0^3}{(\rho g)^2}\left[1+|\bigtriangledown_y|^2\right]\left[|\bigtriangledown_y|-\mu_2\right].\widehat{\nabla}_y \\ &= -n_oC_2A\left[1+|\bigtriangledown_y|^2\right]\left[|\bigtriangledown_y|-\mu_2\right].\widehat{\nabla}_y \end{aligned} \tag{4.20}$$

$$\begin{aligned} J_3 &= -\frac{n_3}{3\eta}\frac{P_0^3}{(\rho g)^2}\left[1+|\bigtriangledown_y|^2\right]\left[|\bigtriangledown_y|-\mu_3\right].\widehat{\nabla}_y \\ &= -\frac{n_oC_3}{3\eta}\frac{P_0^3}{(\rho g)^2}\left[1+|\bigtriangledown_y|^2\right]\left[|\bigtriangledown_y|-\mu_3\right].\widehat{\nabla}_y \\ &= -n_oC_3A\left[1+|\bigtriangledown_y|^2\right]\left[|\bigtriangledown_y|-\mu_3\right].\widehat{\nabla}_y \end{aligned} \tag{4.21}$$

The constant $A = \frac{P_0^3}{3\eta(\rho g)^2}$, $|\bigtriangledown_y|$ is the axial gradient operator and $\widehat{\nabla}_y$ is the unit vector in the opposite direction of steepest descent, at a point on the surface. Given that the total concentration is equal to 1, the concentration of the third species (C_3) can be eliminated using $C_3 = 1-(C_1+C_2)$. The terms can then be rearranged such that:

$$\begin{aligned} &[(1-C_1)j_1 - C_1[j_2+j_3]] = \\ &\qquad n_oA\left[1+|\bigtriangledown_y|^2\right]\left[C_1^2\left[\mu_3-\mu_1\right]+C_1C_2\left[\mu_3-\mu_2\right]+C_1\left[\mu_1-\mu_3\right]\right] \end{aligned} \tag{4.22}$$

$$[(1-C_2)j_2 - C_2[j_1+j_3]] = n_o A\left[1+\mid \bigtriangledown_y \mid^2\right]\left[C_2^2\left[\mu_3-\mu_2\right]+C_1C_2\left[\mu_3-\mu_1\right]+C_2\left[\mu_2-\mu_3\right]\right] \tag{4.23}$$

The following equations were obtained after Eq. 4.22 and Eq. 4.23 were substituted into Eq. 4.17 and Eq. 4.18 respectively:

$$\left.\begin{aligned}\frac{\partial}{\partial t}C_1 &= -\frac{1}{n_o}\frac{\partial}{\partial z}\int_{surface} n_o A\left[1+\mid \bigtriangledown_y \mid^2\right]\left[C_1^2\left[\mu_3-\mu_1\right]+C_1C_2\left[\mu_3-\mu_2\right]+C_1\left[\mu_1-\mu_3\right]\right].\widehat{\nabla}_y \\ \frac{\partial}{\partial t}C_2 &= -\frac{1}{n_o}\frac{\partial}{\partial z}\int_{surface} n_o A\left[1+\mid \bigtriangledown_y \mid^2\right]\left[C_1C_2\left[\mu_3-\mu_1\right]+C_2^2\left[\mu_3-\mu_2\right]+C_2\left[\mu_2-\mu_3\right]\right].\widehat{\nabla}_y\end{aligned}\right\} \tag{4.24}$$

Application of the first order approximation to the axial gradient operator in a binomial expansion yields the axial component as:

$$\mid \bigtriangledown_y \mid = y_x \quad \text{and} \quad \widehat{\nabla}_y = \left(\frac{y_z}{y_x}\right) .$$

Then Eqs. 4.24 becomes:

$$\left.\begin{aligned}\frac{\partial}{\partial t}C_1 &= A\frac{\partial}{\partial z}\int_{surface}\left[1+y_x^2\right]\left\{C_1^2(\mu_1-\mu_3)+C_1C_2(\mu_2-\mu_3)+C_1(\mu_3-\mu_1)\right\}\left(\frac{y_{z_1}}{y_x}\right) \\ \frac{\partial}{\partial t}C_2 &= A\frac{\partial}{\partial z}\int_{surface}\left[1+y_x^2\right]\left\{C_1C_2(\mu_1-\mu_3)+C_2^2(\mu_2-\mu_3)+C_2(\mu_3-\mu_2)\right\}\left(\frac{y_{z_2}}{y_x}\right)\end{aligned}\right\}$$

The derivative dy/dz can only be written through $C(z)$ [7, 11] as:

$$y_z = \frac{\partial y}{\partial z} = \frac{\partial y}{\partial C}\frac{\partial C}{\partial z} = y_C\frac{\partial C}{\partial z} \tag{4.25}$$

Eventually, we get a coupled system of non-linear partial differential equations (PDEs) given by:

$$\frac{\partial C_1}{\partial t} = A\left[\left[1+y_x^2\right]\left[\frac{y_C}{y_x}\right]\frac{\partial}{\partial z}\left[C_1^2\left[\mu_3-\mu_1\right]+C_1\left[\mu_1-\mu_3\right]+C_1C_2\left[\mu_3-\mu_2\right]\right]\frac{\partial C_1}{\partial z}\right] \tag{4.26}$$

$$\frac{\partial C_2}{\partial t} =$$
$$A\left[\left[1+y_x^2\right]\left[\frac{y_C}{y_x}\right]\frac{\partial}{\partial z}\left[C_2^2\left[\mu_3-\mu_2\right]+C_2\left[\mu_2-\mu_3\right]+C_1C_2\left[\mu_3-\mu_1\right]\right]\frac{\partial C_2}{\partial z}\right] \quad (4.27)$$

4.3.2 Four Species Mixture

Following the same argument of segregation instability that was applied in Section 4.3.1, the set of PDEs that represents axial segregation of four species mixture can be expressed as:

$$\frac{\partial}{\partial t}C_1 = A\left[1+y_x^2\right]\left[\frac{y_C}{y_x}\right]\frac{\partial}{\partial z}$$
$$\left[C_1^2(\mu_1-\mu_4)+C_1C_2(\mu_2-\mu_4)+C_1C_3(\mu_3-\mu_4)+C_1(\mu_4-\mu_1)\right]\frac{\partial C_1}{\partial z} \quad (4.28)$$

$$\frac{\partial}{\partial t}C_2 = A\left[1+y_x^2\right]\left[\frac{y_C}{y_x}\right]\frac{\partial}{\partial z}$$
$$\left[C_1C_2(\mu_1-\mu_4)+C_2^2(\mu_2-\mu_4)+C_2C_3(\mu_3-\mu_4)+C_2(\mu_4-\mu_2)\right]\frac{\partial C_2}{\partial z} \quad (4.29)$$

$$\frac{\partial}{\partial t}C_3 = A\left[1+y_x^2\right]\left[\frac{y_C}{y_x}\right]\frac{\partial}{\partial z}$$
$$\left[C_1C_3(\mu_1-\mu_4)+C_2C_3(\mu_2-\mu_4)+C_3^2(\mu_3-\mu_4)+C_3(\mu_4-\mu_3)\right]\frac{\partial C_3}{\partial z} \quad (4.30)$$

4.3.3 Generalization to $n-$species mixture

For a mixture of multi-species (n) one can present the corresponding set of PDEs of axial segregation as follows:

- The number of the equations is given by $n-1$, where n is the number of the species of different types used in the mixture. The reduction to $n-1$ equations results from:

$$C_n = 1-(C_1+C_2+C_3+....+C_{n-1})$$

.

- The set of the equations is given by:

$$\left.\frac{\partial C_n}{\partial t}\right|_{n=1}^{n-1} = \underbrace{\left\{A\left[1+y_x^2\right]\left[\frac{y_{C_n}}{y_x}\right]_{n=1}^{n-1}\right\}}_{\text{diffusion coefficient}} \frac{\partial}{\partial z}\left[\left|C_n\right|_{n=1}^{n-1}\sum_{n=1}^{n-1}\left[C_n(\mu_n-\mu_m)\right] + \left|C_n(\mu_m-\mu_n)\right|_{n=1}^{n-1}\right]\left.\frac{\partial C_n}{\partial z}\right|_{n=1}^{n-1},$$

where μ_m is the highest friction coefficient of the species in the mixture.

For example, for five species mixture (that is $n = 5$ and $\mu_m = \mu_5$) we get the following four equations:

$$\frac{\partial C_1}{\partial t} = \left\{A\left[1+y_x^2\right]\left[\frac{y_{C_1}}{y_x}\right]\right\}\frac{\partial}{\partial z}\left\{C_1^2(\mu_1-\mu_5)+C_1C_2(\mu_2-\mu_5)+C_1C_3(\mu_3-\mu_5)+C_1C_4(\mu_4-\mu_5)+C_1(\mu_5-\mu_1)\right\}\frac{\partial C_1}{\partial z}$$

$$\frac{\partial C_2}{\partial t} = \left\{A\left[1+y_x^2\right]\left[\frac{y_{C_2}}{y_x}\right]\right\}\frac{\partial}{\partial z}\left\{C_1C_2(\mu_1-\mu_5)+C_2^2(\mu_2-\mu_5)+C_2C_3(\mu_3-\mu_5)+C_2C_4(\mu_4-\mu_5)+C_2(\mu_5-\mu_2)\right\}\frac{\partial C_2}{\partial z}$$

$$\frac{\partial C_3}{\partial t} = \left\{A\left[1+y_x^2\right]\left[\frac{y_{C_3}}{y_x}\right]\right\}\frac{\partial}{\partial z}\left\{C_1C_3(\mu_1-\mu_5)+C_2C_3(\mu_2-\mu_5)+C_3^2(\mu_3-\mu_5)+C_3C_4(\mu_4-\mu_5)+C_3(\mu_5-\mu_3)\right\}\frac{\partial C_3}{\partial z}$$

$$\frac{\partial C_4}{\partial t} = \left\{A\left[1+y_x^2\right]\left[\frac{y_{C_4}}{y_x}\right]\right\}\frac{\partial}{\partial z}\left\{C_1C_4(\mu_1-\mu_5)+C_2C_4(\mu_2-\mu_5)+C_3C_4(\mu_3-\mu_5)+C_4^2(\mu_4-\mu_5)+C_4(\mu_5-\mu_4)\right\}\frac{\partial C_4}{\partial z}$$

4.4 Determination of the axial flow: $\frac{dy}{dC}$

The derivative dy/dC is another important parameter that needs to be calculated in order to obtain the diffusion coefficient associated with all the diffusion equations presented in this thesis. As presented in [11], this derivative can be obtained from the following equation:

$$\frac{dy}{dC} = \frac{dy}{dz}\frac{dz}{dC}\,. \tag{4.31}$$

The partial derivative can then be calculated as:

$$\frac{dy}{dC} = \frac{y(x,z+\delta z)-y(x,z)}{C(z+\delta z)-C(z)}\,. \tag{4.32}$$

It is easy to obtain the derivative $\frac{dC}{dz}$ which represents the fluctuations in relative concentration of the species in the mixture along the drum axis (z-axis). A Fourier series expansion was used to represent the function $C(z)$ in form of a square-sine

function expressed as the following sum of odd harmonics:

$$C(z) = \sum_{1}^{n} \frac{\sin(nz)}{n} \,, \tag{4.33}$$

where n is the number of odd harmonics. Fig. 4.5 shows the concentration C as a function of z using Eq. 4.33 with $n = 19$.

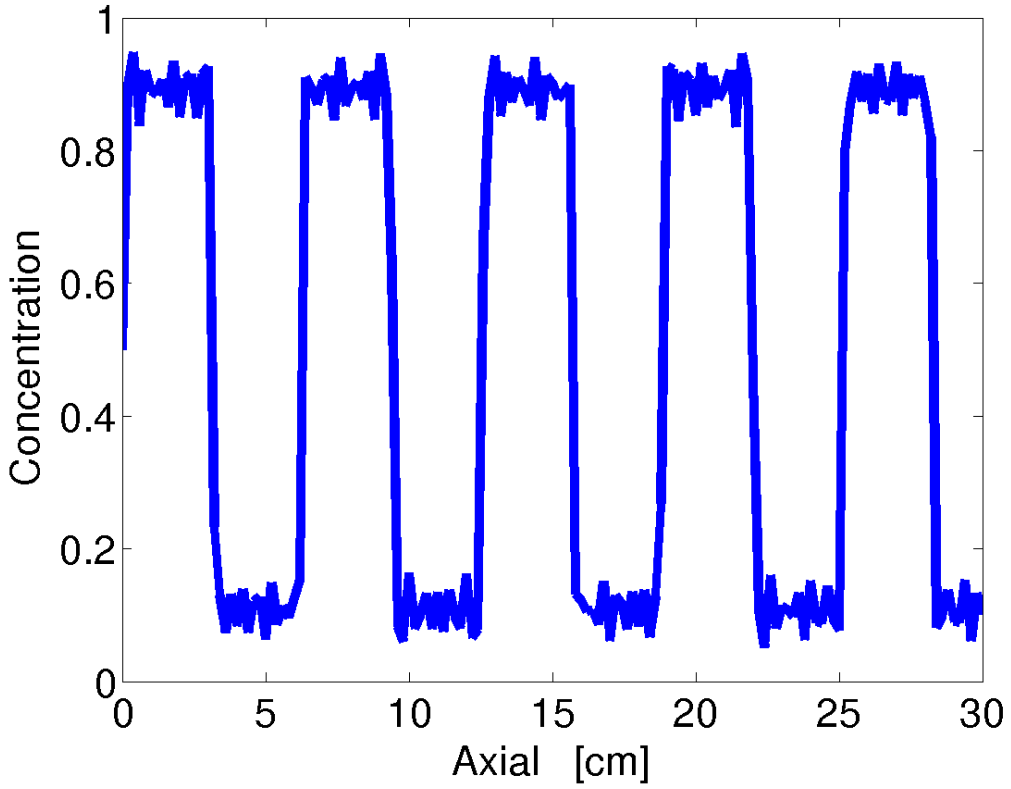

FIGURE 4.5: The behavior of the concentration of species in the mixture along the drum axis. The square-sine wave was obtained using Fourier series expansion of a sum of odd harmonics up to $n = 19$.

Consequently, the challenge is to calculate the axial surface profiles (dy/dz) which are rarely discussed in literature [67]. We relied on two descriptions to be able to obtain the axial surface profiles. These descriptions are relatively similar. The first description is the measured axial surface profile formula. The formula was presented by [67]. They described the axial profiles as parabolic curves along the drum axis. The formula is given by:

$$y(x, z) = y_x + \frac{a_z}{2}\left(z - \frac{1}{2}\right)^2 \,, \tag{4.34}$$

where y_x is the surface height at the axial centerline, a_z is the axial surface curvature on the axial plane and L is the width (length) of the drum. The second description is a fit of data introduced by [68] and can be expressed as:

$$< \Theta(z) >= \Theta_\infty + \Delta\Theta \left(e^{-z/\zeta} + e^{-(L-z)/\zeta} \right), \tag{4.35}$$

where Θ is the dynamic angle of repose, Θ_∞ is the dynamic angle of repose far away from the boundaries (at the middle), $\Delta\Theta$ is the angular difference between the value at the boundary and at the middle (Θ_∞) and ζ is a characteristic length.

We combined these two equations by replacing the $(a_z/2)$ term with height difference between the value at the boundary y_{end} and at the middle y_{mid}. This combination circumvents the need for explicit knowledge of the axial surface curvature, a_z. The result of the combination is as follows:

$$y(x,z) = y_x + (y_{end} - y_{mid}) \left(z - \frac{1}{2} \right)^2. \tag{4.36}$$

Fig. 4.6 shows axial surface profiles using Eq. 4.34 (with different values of a_z) and Eq. 4.36.

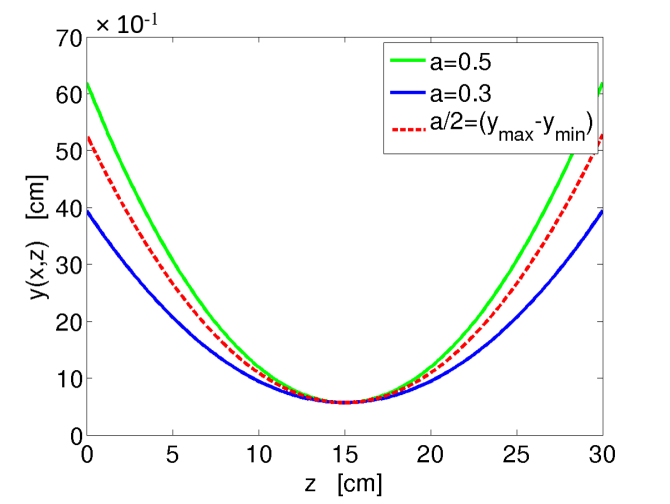

FIGURE 4.6: Axial surface profiles for different values of surface curvature: $a_z = 0.5$ (green line) and $a_z = 0.3$ (blue line) and from the combined formula showed in Eq. 4.36 (red dashed line).

4.5 Initiation of axial segregation in rotating drums

Consistent with our hypothesis, we select the concentration anisotropy at time $t = 0$ to match heuristic criteria for tumbling mills. The reasoning is as follows: Typical tumbling mills employed in the mineral processing industry have conical end caps, which is equivalent to saying that the drum radius decreases linearly along the end-caps as you move away from the axial centre of the drum. According to experimental findings by [11] for drum fillings $\leq 50\%$, smaller particles accumulated in the narrower sections (smaller radius) of their periodically modulated drum. In terms of our friction hypothesis this implies that if two adjacent axial sections of different radii are presented with a frictional mixture of grains, the tendency will be for the lower radii section to contain more of the higher friction species than the adjacent (higher radius) section. Accordingly, the concentration of higher (respectively, lower) friction species should be higher (respectively, lower) in the smaller radial section than the adjacent larger radial section. So if an initially uniform mixture was rotated in a drum with conical end caps (a typical tumbling mill), after a short while we can expect the mixture to segregate in the conical end caps such that the average friction varies inversely with end cap radius. And for a Bagnoldian free surface—see Fig. (3.11)—this implies that the average height of the free surface should then vary inversely with end cap radius. To test this conclusion, we plot the variation of the Bagnoldian free surface profile with radius; see Fig. (4.7): The plot clearly confirms that the height of the free surface varies inversely with the drum radius for the Bagnoldian free surface, i.e. the height of the free surface increases with decreasing drum radius.

Two axial segregation configurations can be imagined for this scenario:

(i) The end caps are rich in low friction species.

(ii) The end caps are rich in high friction species.

Configuration (i) leads to axial slopes that are inclined towards the drum centre and thus initial segregation is directed inwards while configuration (ii) achieves the opposite. Configuration (i)—the configuration that we investigate in this section—is of greater practical value as it initiates the segregation process into the main chamber of the drum. As initiation of axial segregation is the focus in this section, we limit the results to simply confirming if bands form or not, thereby

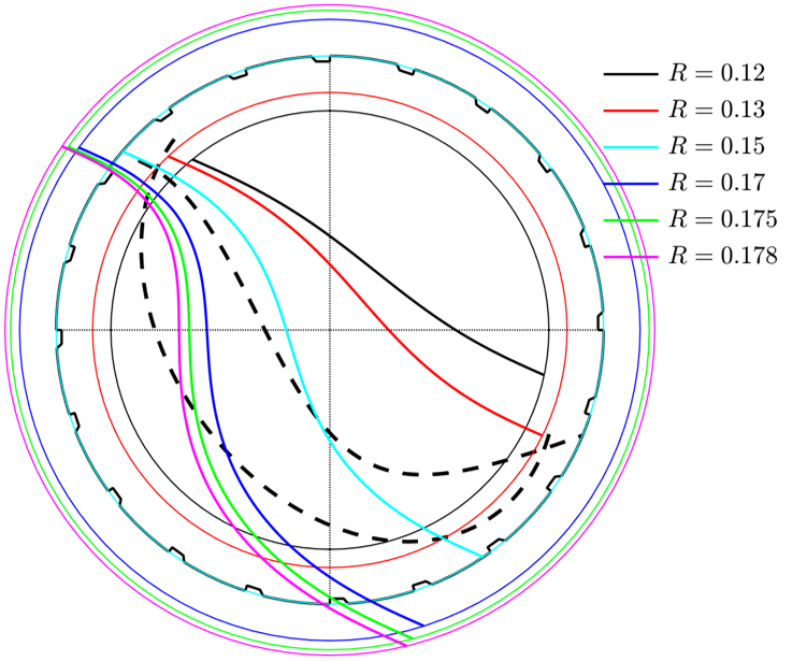

FIGURE 4.7: Variation of the Bagnoldian free surface profile with drum radius. All other parameters used for the fit are are given in Table (3.1).

establishing the minimum concentration anisotropy conditions required to initiate axial segregation up to band formation. The next chapter will comprise longer simulations as both banding and band coarsening are sought.

Consider a binary mixture as depicted in Fig. 4.8, where one of the two friction species, with concentration C, has a lower and linearly varying concentration near the end-walls.

This initial condition was obtained with the following function:

$$C(z, t=0) = \begin{cases} 0.99 & : z > 1 \quad \& \quad z < z_{\max} - 1 \\ 0.50 & : \text{elswhere;} \end{cases}$$

where $z = 285$ cm is length of the drum along the axis of rotation and t represents the time. Fig. 4.9 shows the corresponding axial segregation result for a Bagnoldian free surface profile and a first order expansion of the axial gradient operator. Accordingly, no band coarsening is expected or sought.

As presented in Fig. 4.9(a) many bands are obtained when the variation in concentrations is high and and no bands appear when the difference in concentration is low as showed in Fig. 4.9(b). Table. 4.1 shows the range of variation in the

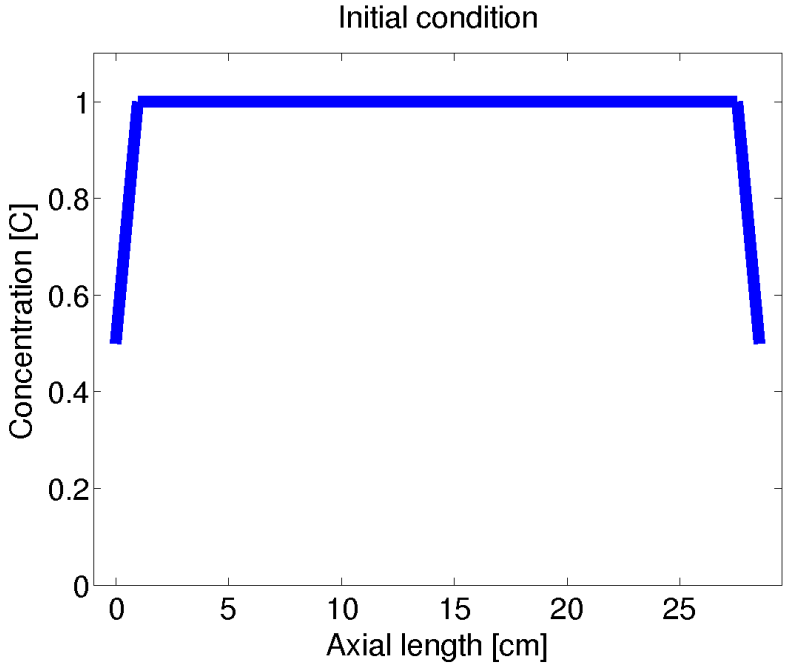

FIGURE 4.8: The initial condition of small concentration variations near the axial end-walls.

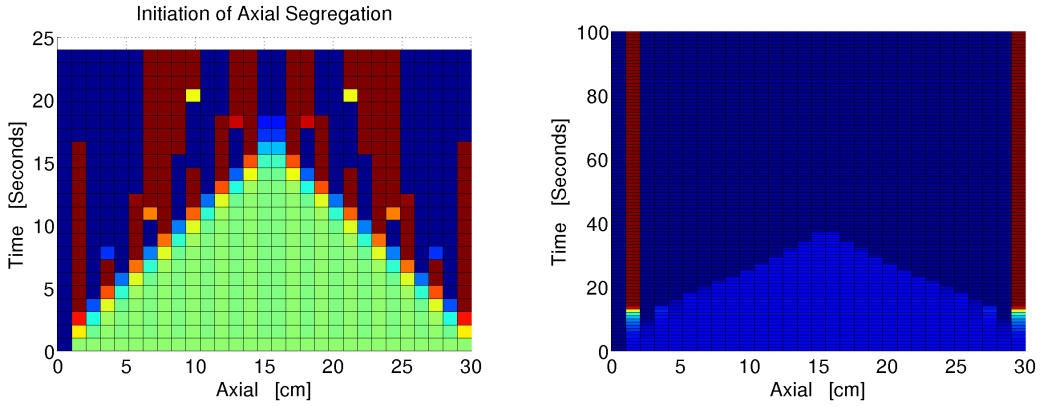

(a) High difference in concentration.

(b) Low difference in concentration.

FIGURE 4.9: Space-time plots of the numerical solution corresponding to the initial condition. The maximum concentration away from the end-walls is 0.99 while near the end-walls: (a) $C = 0.50$ (many bands appear), (b) $C = 0.90$ (no bands appear). The green colour refers to the mixed state which clearly starts disappearing with time evolution in favour of banding (burgundy colour).

concentration (C) of one of the two friction species at the end-walls of the drum and anywhere else.

Away from end-walls	**Near end-walls**	**Remarks**
0.99	1.0	No bands
0.99	0.9	No bands
0.99	0.8	Very few bands
0.99	0.7	Few bands
0.99	0.6	Good number of bands
0.99	0.5	Many bands

TABLE 4.1: The range of variation in concentration (C) of one of the two friction species and its effect on band formation.

4.6 Summary

In this chapter we presented the mechanism for axial segregation. An important distinction between adjacent axial slices was observed for Bagnoldian and Newtonian formulations:

1. Newtonian gravity slopes are directed from high-to-low friction species in the upper section (above the inflection point) while the exact opposite is observed below the inflection point. The net effect is to counteract axial diffusion unless significant differences in frictional properties exist between adjacent layers.

2. Bagnoldian gravity slopes are unidirectional and always from high-to-low friction species. This adds credence to the friction hypothesis and obviates the need for complicated explanations like travelling waves and spinodal decomposition [11] that do not have practical implementations in real systems like tumbling mills.

Motivated by the need to capture band coarsening, the multidirectional axial gradient operator was binomially expanded to second order. As will become apparent in the next chapter, this increases the sensitivity of the diffusion coefficient sufficiently to force the segregation beyond initial banding to eventual band coarsening. In terms of granular mixtures (by frictional properties) explicit solutions are given for binary, ternary, quaternary and the general n-species mixtures. Finally, a derivation for $\frac{dy}{dC}$ is presented wherein the hard-to-measure axial surface curvature (a_z) is circumvented by use of an empirical result [68].

Finally, the initiation of band formation for a Bagnoldian free surface profile with a first order axial gradient operator was demonstrated for different concentrations of a bimodal mixture comprising two friction species. In general, a good number of bands form when the concentration difference between regions is greater than 0.39. No bands form if the concentration difference is less than 0.09. The initial concentration profile considered here is an ideal representation of the concentration distribution in tumbling mills that have the characteristic conical end caps. The height of the Bagnoldian free surface profiles vary inversely with drum radius. Along the conical end caps, this leads to axial gravity slopes along which particles can flow from the relatively higher frictional surface to the relatively lower surface. This is the mechanistic source of the segregation, with the extent of the segregation determined by the differences in average friction, and of course their relative concentrations.

Chapter 5

Result and Discussion

5.1 Introduction

In this chapter we present the results of axial segregation in a rotating drum with space-time diagrams for bimodal ($n = 2$) species and axial concentration profiles for ($n = 3,\ 4$) species. The numerical solutions are performed in Matlab using the ODE and PDE toolboxes. Space-time diagrams represent grains with similar frictional properties by individual colour bands that span space (horizontal axis) and time (vertical axis)—This is the axial banding pattern that we seek to prove our hypothesis. The analysis is restricted to the optimised experimental configuration parameters described in Sections (3.3 & 3.6), and the related solutions of the Bagnoldian free surface model described in Sections (A.3 & A.4). In particular, the boundary conditions from Chapter (3) implicitly restrict our simulations to drums fillings less than 50% as this configuration extends the body of knowledge beyond the literature surveyed in this thesis. Initial boundary conditions for the concentration are set according to the allowed range identified in Section (4.5) and are thus consistent with tumbling mill concentrations. All parameter variation is restricted according to the viable ranges identified in Chapter (3). To quantitatively assess the individual parameters and the mathematical extensions employed in this thesis, separately, the analysis is split into the following categories:

1. First we present the solutions of the Bagnoldian diffusion equation by testing the sensitivity of the model to the different parameters affecting band

formation. As stable band coarsening only occurs in the long time limit (in $\sim$ 100 simulated seconds, which takes several hours in real time on a standard desktop PC), the parametric analysis was performed for simulation times significantly less than 100 seconds ($\sim$ 30 simulated seconds) to ensure that significant band coarsening is not reached. This allows us to make assessments of the number of bands formed as a consequence of varying the above-mentioned parameters. In most configurations the simulation time is set at 30 seconds, except for the short drum lengths that require more simulation time ($\sim$ 50 simulated seconds) to yield discernable banding. Accordingly, the results are analysed in terms of:

(a) mechanical properties of the grain (size or particle diameter, solids concentration[1] and average friction),

(b) drum geometry (diameter, length, end-wall friction), and

(c) operating conditions (drum rotation rate).

2. Then, we test the influence of the binomially expanded gradient operator, as given by equation Eq. A.38, on band coarsening. In particular, we evolve the solution multiple times, increasing the time of simulation for each test to quantitatively examine the evolution of band coarsening.

3. Lastly, we present the solutions of axial segregation for multi-species mixture. These include the solution of the set of equations presented in Section 4.3.1 (Eqs. 4.26 and 4.27) and Section 4.3.2 (Eqs. 4.28, 4.29 and 4.30) of Chapter 4, for ternary and quaternary mixtures, respectively. The aim here is to recover non-linear banding (bands within bands, etc) as experimentally observed in the literature but for drum fillings $< 50\%$.

5.2 Role of mechanical properties

The variation in the mechanical properties of the grain were bound by the observations made in Chapter (3): For a drum filling less than 50%, realistic free surface profiles were obtained provided that we restrict the average friction to the range $\mu \in [0.1;\ 0.5]$. The grain density (ρ_m)—which forms part of our hypothesis formulation—comes into the formulation via the bulk density relation: $\rho = \phi\rho_m$ where

[1] This relates directly to the material density of the grains

we initially set the volume concentration $\phi = 0.6$ in the free surface modelling. We thus indirectly account for the influence of grain density by changing (in our case, reducing) the volume fraction from $\phi = 0.6$ down to $\phi = 0.4$. For $\phi < 0.4$ the bed is fully fluidised and the free surface models (Bagnoldian and Newtonian) should not be valid.

For the variations in grain size and volume fraction, the average friction (μ) was set to the middle of the viable range,i.e. $\mu = 0.3$, to ensure that the free surface profile produces a bed span of $< 50\%$ of drum volume for all variations of the parameters. Other simulation parameters are consistent with the optimised parameter set defined in Table (3.1). Our physical situation is thus nominally based on the experimental configuration described in Section (3.3), with necessary changes to limit bed span to $< 50\%$ of drum volume.

5.2.1 Effect of grain size (d)

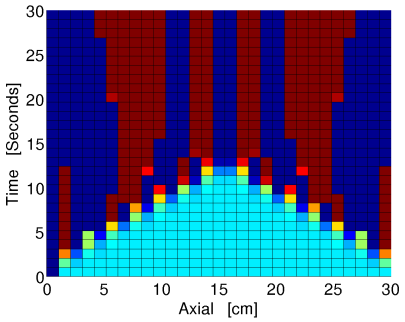

(a) The smallest grain size ($d = 3$ mm) produces the most bands.

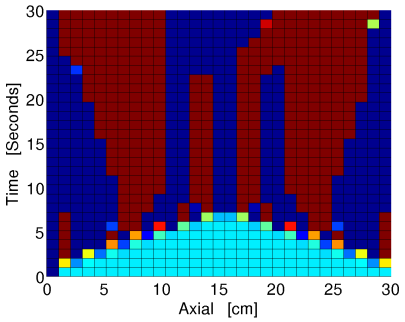

(b) At $d = 5$ mm, the number of bands reduced when compared to $d = 3$ mm.

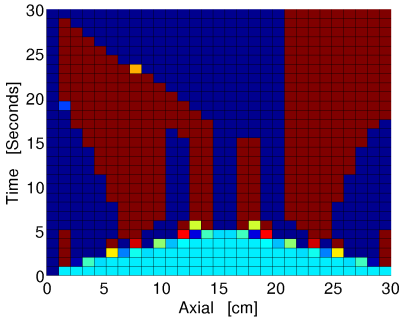

(c) The largest grain size of $d = 7$ mm produces the smallest number of bands.

FIGURE 5.1: Influence of grain size on the axial band formation. The number of bands are inversely proportional to the grain size (d), i.e. the most bands are obtained when $d = 3$ mm (Fig. 5.1(a)) with the least number of bands occurring for the largest size of $d = 7$ mm (Fig. 5.1(c)). The onset of clear band formation also appears sooner when d is increased.

5.2.2 Effect of volume fraction (ϕ)

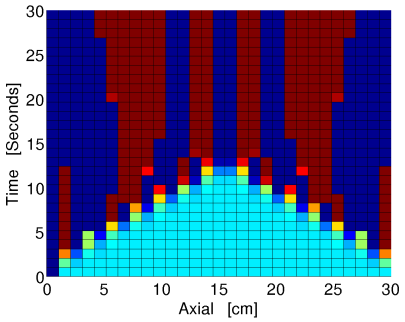

(a) $\phi = 0.6$: Many different bands.

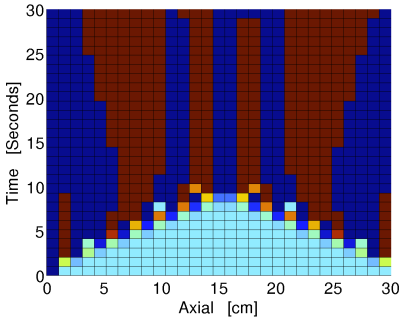

(b) $\phi = 0.5$: An observable decrease in the number of bands.

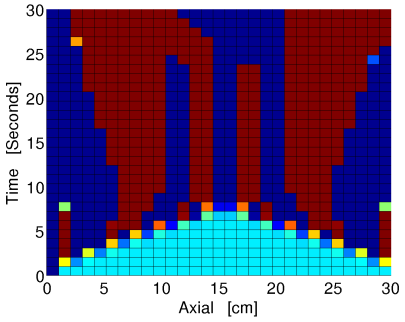

(c) $\phi = 0.4$: The least number of bands observed.

FIGURE 5.2: Influence of volume fraction on the axial band formation. The number of bands progressively decrease with a corresponding decrease in ϕ. 5.2(a) shows a relatively high number of bands. 5.2(b) depicts a decrease in the number of bands. 5.2(c) has the least number of bands. Clear band formation starts to appear sooner with lower values of ϕ.

5.2.3 Effect of average friction (μ)

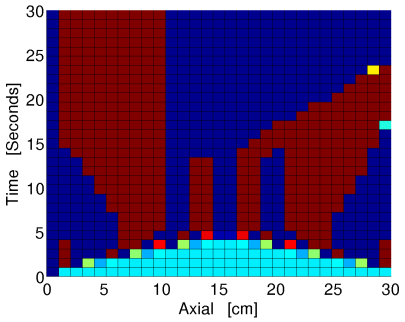

(a) $\mu = 0.3$ and the sharp bands obtained after 5 seconds.

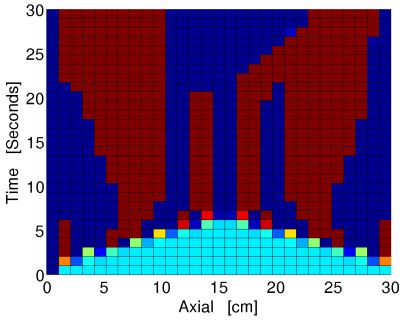

(b) $\mu = 0.2$ and the sharp bands obtained after 7 seconds.

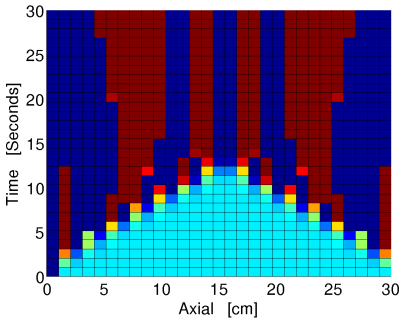

(c) $\mu = 0.1$ and the sharp bands obtained after 13 seconds.

FIGURE 5.3: The influence of average friction (μ) on band formation. There is an inverse relation between the average grain friction and initiation time to clear band formation with the shortest time needed for high friction ($\mu = 0.3$ in Fig. 5.3(a)) and longest time for the lowest friction ($\mu = 0.1$ in Fig. 5.3(c)).

5.3 Role of drum geometry and speed

5.3.1 Effect of the drum diameter $(D = 2R)$

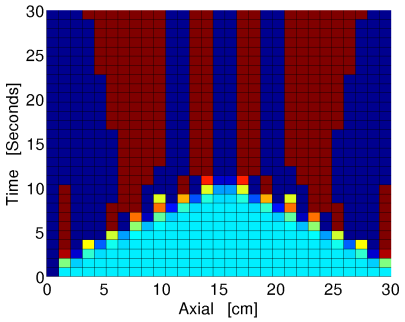

(a) $R = 17$ cm: Many clear bands appear.

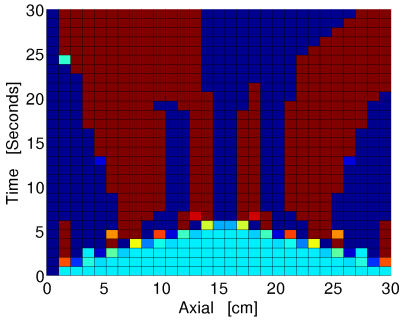

(b) $R = 15$ cm: Fewer clear bands appear.

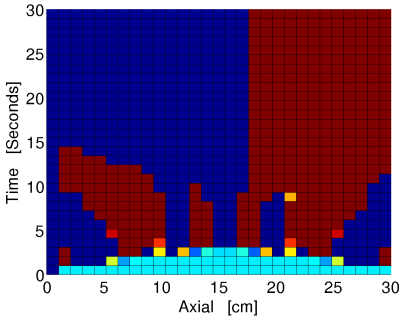

(c) $R = 13$ cm: Least amount of clear bands appear.

FIGURE 5.4: The influence of drum diameter $(D = 2R)$ on band formation. The number of bands are proportional to the drum diameter. More bands are obtained when $R = 17$ cm (Fig. 5.4(a)) while the least number of bands form for the smallest drum $(R = 13$ cm) as seen in Fig. 5.4(c).

5.3.2 Effect of the drum length (W)

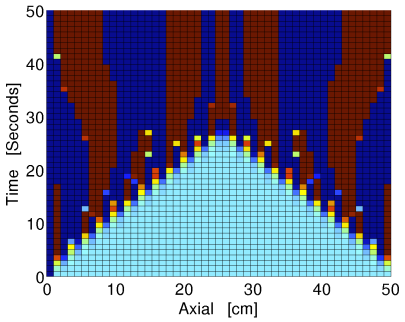

(a) $W = 50$ cm: Many clear bands.

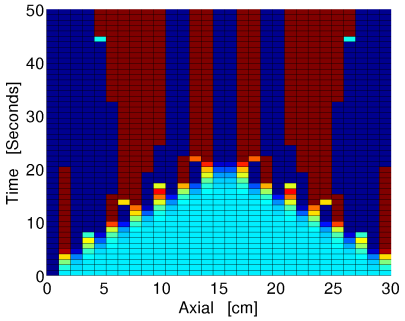

(b) $W = 30$ cm: Slightly less bands than for $W = 50$ cm.

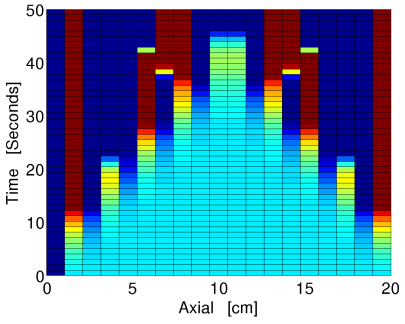

(c) $W = 20$ cm: Fewer clear bands.

FIGURE 5.5: The influence of drum length (W) on band formation. The number of bands are directly proportional to the drum length (W). The most bands are obtained when $W = 50$ cm (see Fig. 5.5(b)) and least for $W = 20$ mm; see Fig. 5.5(c).

5.3.3 Effect of end-wall friction (μ_w)

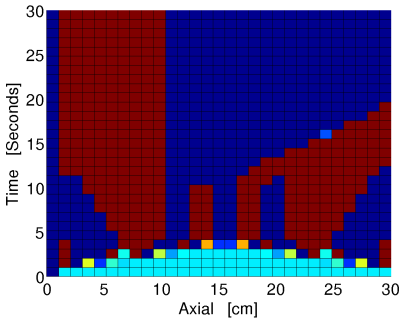

(a) $\mu_w = 0.45$: Clear bands appear after 4 seconds.

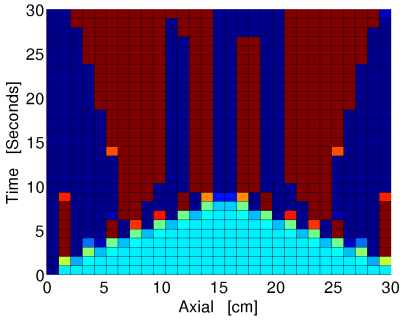

(b) $\mu_w = 0.55$: Clear bands appear after 9.0 seconds.

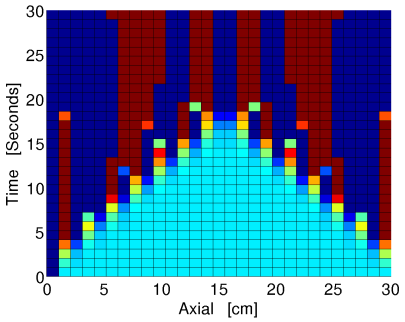

(c) $\mu_w = 0.65$: Clear bands appear after 19 seconds.

FIGURE 5.6: The influence of wall friction (μ_w) on band formation. Increasing the wall-friction delays the onset of clear band formation: Only 4 seconds needed to obtain clear bands when $\mu_w = 0.45$ (see Fig. 5.6(a)) and 19 seconds when $\mu_w = 0.65$; see Fig. 5.6(b).

5.3.4 Effect of drum rotation rate (ω)

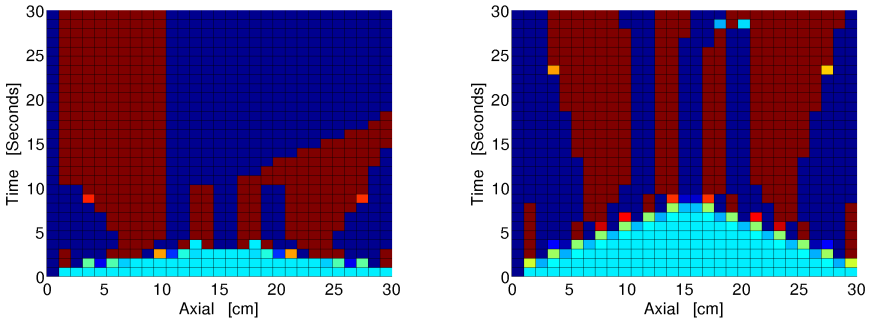

(a) $\omega = 3.0732$ rad/s

(b) $\omega = 3.2350$ rad/s

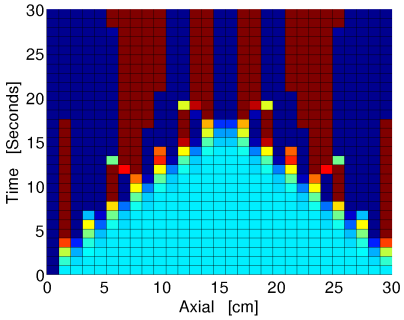

(c) $\omega = 4.0437$ rad/s

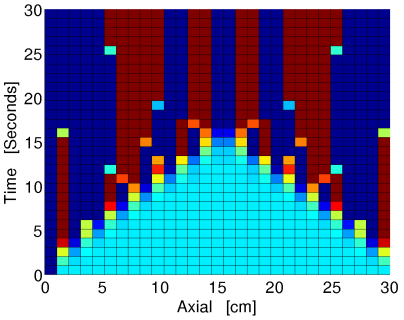

(d) $\omega = 4.8524$ rad/s

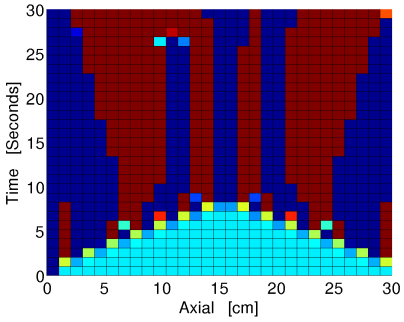

(e) $\omega = 5.8229$ rad/s

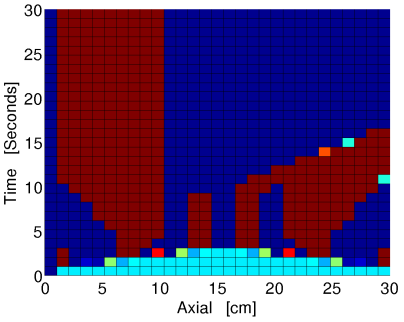

(f) $\omega = 5.9038$ rad/s

FIGURE 5.7: The influence of mill speed (ω) on band formation. The number of bands increases with a corresponding increase in the rotation rate (Fig. 5.7(b) and Fig. 5.7(c)) and then remains constant for further speed increases (Fig. 5.7(d)) before it finally decreases at high speeds (Fig. 5.7(e) and Fig. 5.7(f)).

5.4 Coarsening effect

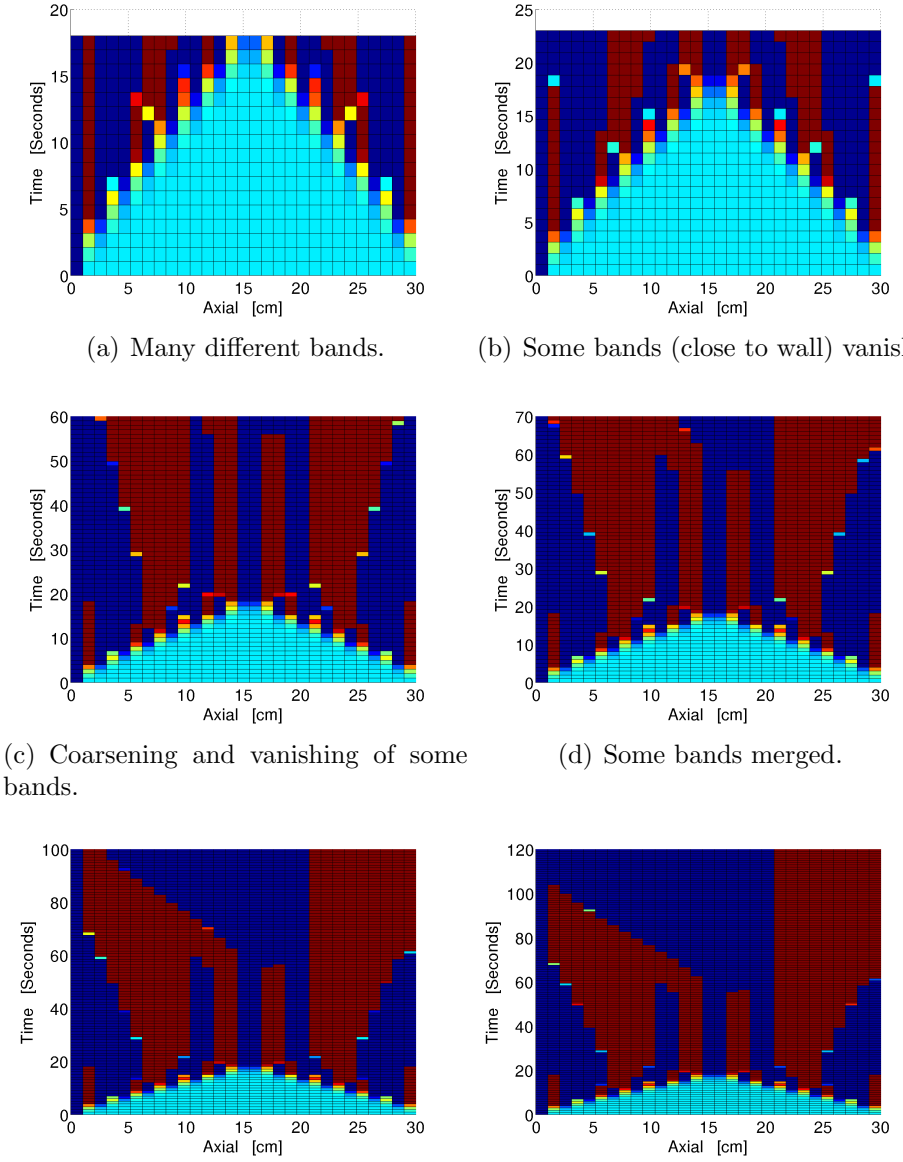

(a) Many different bands.

(b) Some bands (close to wall) vanish.

(c) Coarsening and vanishing of some bands.

(d) Some bands merged.

(e) Coarsening.

(f) Coarsening and vanishing of some bands.

FIGURE 5.8: Recovery of band coarsening in the long time limit. Some bands vanish and merge, leading to eventual band coarsening that eventually stabilises at around 100 seconds of simulation time.

5.5 Multi-species mixtures

5.5.1 Boundary condition

The following two simple equations can be used to initiate the axial banding:

$$C_{upper} - C_{lower} = \frac{1}{n} \tag{5.1}$$

$$(n-1) * C_{lower} + C_{upper} = 1, \tag{5.2}$$

where n is the number of different-frictional species used in the mixture and C_{upper} and C_{lower} represent, respectively, the upper and lower boundaries of the concentration (C) at the initial state. In case of three species mixture, where $n = 3$, the lower and upper limits of the concentration are 0.225 and 0.550 respectively as presented in Fig. 5.9 below.

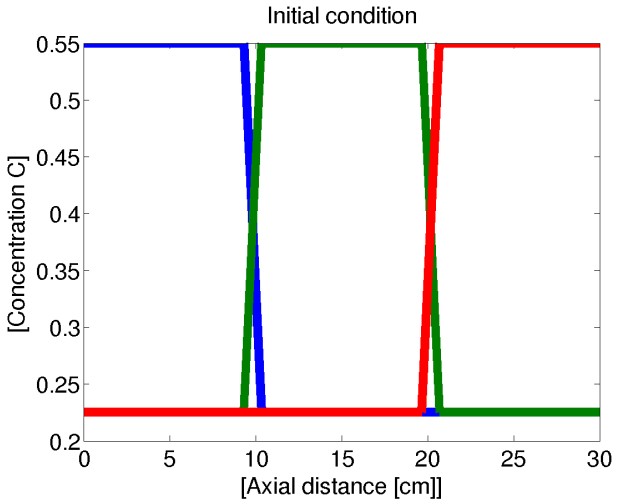

FIGURE 5.9: Initial conditions according to equations 5.1 and 5.2. The three different colors refer to the three different-frictional species.

5.5.2 Results

The solutions of the set of the PDEs must be normalized as the two limits of the concentration are shifted up. It is clearly seen from Fig. 5.9 that the lower and the upper limits are shifted up by 0.225 which has to be taken into account in the discussion of the result. Using these two equations allows initial states where all the components of the mixture are proportionately represented across the full

axial span of the drum. For example, in the case of three species (Fig. 5.9), each component occupies one third of the drum. Fig. 5.10 and Fig. 5.11 show the solution of the initial axial banding associated with ternary and quaternary mixtures, respectively.

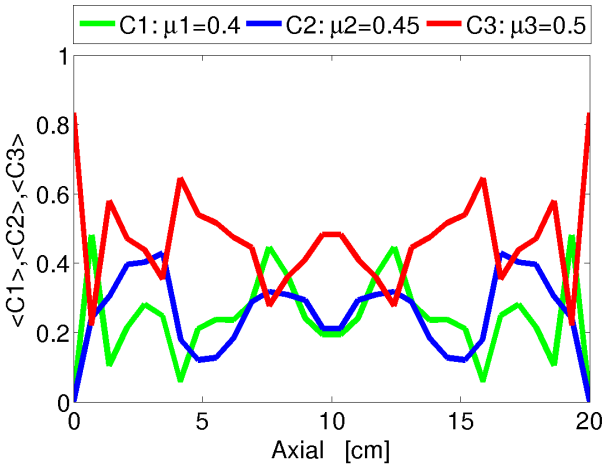

FIGURE 5.10: The numerical solution of equations 4.26 and 4.27. Bands within bands. The three different colors refer to the three different-frictional species.

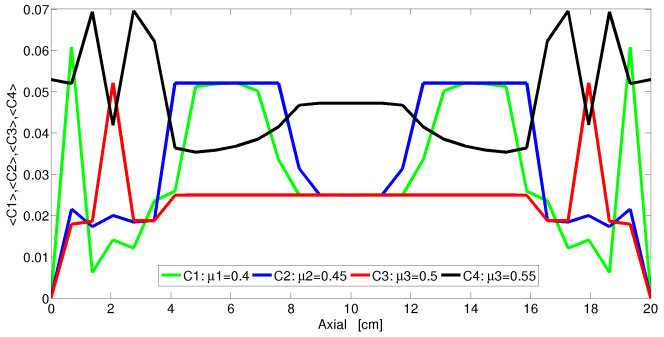

FIGURE 5.11: The numerical solution of equations 4.28, 4.29 and 4.30. Bands within bands within bands. The four different colors refer to the four different-frictional species.

5.6 Discussion

Space-time plots of the Bagnoldian-based axial segregation model was presented in this chapter through a series of parametric investigations spanning mechanical properties and drum geometry. The parametric variations are consistent with drum fillings less than 50% and performed for fixed time evolutions. The influence of these parameters on band formation are summarised in Table (5.1). The results are consistent with experimental findings reported in the literature [35].

Increased parameter	**Effect on axial segregation**	**Figure**
Particle size (d)	decrease the number of bands	Fig. 5.1
Volume fraction (ϕ)	decrease the number of bands	Fig. 5.2
Average friction (μ)	decrease the number of bands	Fig. 5.3
Drum diameter (D)	increase the number of bands	Fig. 5.4
Drum length (W)	increase the number of bands	Fig. 5.5
End-wall friction (μ_w)	increase the number of bands	Fig. 5.6

TABLE 5.1: The effect of increasing individual parameter on the diffusion coefficient and consequently the formation of clear bands.

An interesting set of space-time plots was obtained when the drum rotation rate was varied across a wide range of the Froude regime, Fig. 5.7: Starting from low drum rotation rates, the number of bands initially increased with increasing drum speed. With further increases in drum speed, the number of bands reached a maximum and then decreased. The evolution of the number of bands with the rotation rate is summarized in Fig. 5.12. We note that the result agrees with experimental findings by [36] and suggests an optimum speed for maximum banding. Such information can be very useful in industries employing rotating drums to achieve a desired mixture per axial location.

Band coarsening was successfully implemented through higher order extensions of the axial gradient operator. Fig. (5.8) illustrates the space-time plots at different time evolution points. At around 60-70 seconds of simulation time, clear merging and vanishing of bands are apparent. From 100 to 120 simulation seconds, band reduction appears to have stopped, suggesting that the stable band coarsened state has been reached. This result shows good agreement with the experiments performed by [54] and proves our hypothesis of achieving band coarsening through extensions of the axial gradient operator.

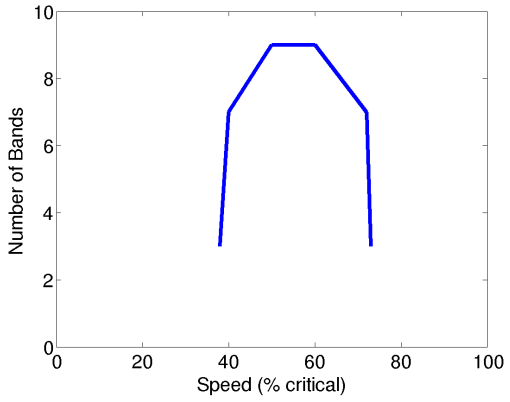

FIGURE 5.12: The evolution of the number of bands with rotation rate.

The importance of the derivative dy/dz is obvious from the fact that small changes in the initial mixture seem to have large effects on the band formation process [69]. These effects hold regardless of how much concentration fluctuations one of the species in the mixture exhibited at the initial state. The result is consistent with the experiments performed by [54].

Beyond binary mixtures, we plot concentration profiles along the axial length of the drum at fixed time evolutions consistent with the time required to reach clear banding ($\sim$ 30 simulation seconds). In this regard, the solutions corresponding to ternary and quaternary mixtures are shown in Figs. (5.10 & 5.11) respectively. The formation of bands within bands is distinct and consistent with literature findings [46]. The only mechanical property that differentiated the species was their friction coefficient (μ_n). We used components with friction coefficients of 0.40, 0.45 and 0.50 in the case of the ternary mixture (Fig. 5.10) and 0.40, 0.45, 0.50, and 0.55 in the case of a quaternary mixture (Fig. 5.11). Changing the friction parameter set naturally produces a different banding pattern as seen in Fig. (5.13) for the quaternary mixture. The formation of bands within bands within bands is a clear indication of a successful result that matches very well the experimental observations by [46] and [38] (see Fig. 2.4 for details). The results also agree with the discrete particle simulations performed by [70].

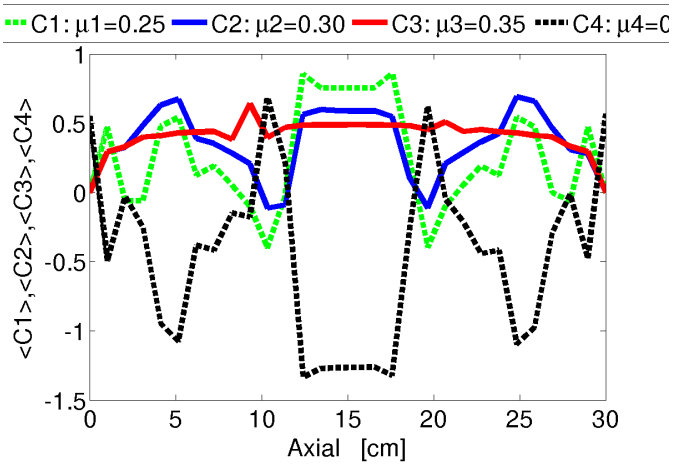

FIGURE 5.13: Band variation in the quaternary mixture that is caused by using a different parameter set of friction values. The four different colors refer to the four different-friction species.

Chapter 6

Conclusion

Motivated by rotating drum model limitations identified in the literature for friction-based axial segregation models of granular mixtures occupying $< 50\%$ of drum volume:

1. Axial banding not recovered.
2. Band coarsening not recovered;

We thus hypothesised that *Granular material composed of different frictional properties diffuse into axial bands due to concentration fluctuations in the Bagnoldian free surface layer caused by friction-limited mobility, and boundary-induced anisotropy in the concentration*; and then successfully tested the development of new models. The main ingredients of the new models are:

(a) The replacement of the Newtonian shear stress with a Bagnoldian formulation of the free surface profile.

(b) The extension of the axial gradient operator to second order.

(c) Generalisation of the Bagnoldian-based axial segregation model to multiple species.

To test the significance of (a), we performed in-situ particle tracking experiments of a representative grain (the tracer) within a drum filled to 30% of it's volume with 5 mm glass beads and rotated at 54 RPM. The nuclear imaging technique of

Positron Emission Particle Tracking (PEPT) was then used to track the trajectory field of the tracer after it was radioactively labelled with a positron emitting isotope (^{68}Ga). For sufficiently long tracking times at steady state operation of the mill, the time averaged behaviour (velocity and volume concentration) of the tracer represents the ensemble average that is consistent with continuum representations of the flow. The free surface profile is clearly and accurately identified from the volume concentration map while the equilibrium surface is numerically extracted from the velocity field. Taken together they facilitated experimental measurement of the free surface profile and bed depth. Least squares fitting of model (a) to the measured profile identified a set of optimised model parameters that set the base case for subsequent analysis. This restriction to a base case is a pragmatic one to allow focus on the model and it's mechanistic implications, and is thus by definition not an exhaustive interrogation of the model(s). The Bagnoldian free surface model was demonstrated to be asymmetric about the inflection point of the S-shaped profile—A property that is necessary to promote axial band formation, even at drum fillings $< 50\%$. Another key observation is the fact that higher average species friction (μ) produce higher free surface profiles, which for adjacent axial layers provides a physical reason (mechanism) to drive axial motion along the natural gravity slope. A subsequent parametric study of the Bagnoldian free surface model also identified clear ranges of parameter validity in relation to the measured profile and our requirement to evolve axial banding for drum fillings $< 50\%$.

The significance of (b) is that while flow down the axial gravity slope exists naturally and consistently for adjacent axial slices described by the Bagnoldian free surface model, greater sensitivity to slope fluctuations are needed to ensure axial band coarsening in the long time limit—A fact that is well observed in the experimental literature.

Initiation of axial segregation requires axial concentration variations to diffusively drive the process. We have argued that for the case of tumbling mills—the industrial application of rotating drums—geometric variations along the drum length (like the use of conical end caps in the mining industry) is sufficient to seed the initial concentration anisotropy.

In an attempt to describe realistic mixtures of frictional species, i.e. more than $n = 2$ species, we successfully extended the formulation of the axial segregation model to $n-$species with explicit representations of $n = 2,\ 3,\ 4$.

A parametric study of the new axial segregation model was then performed and successfully shown to recover:

1. Initial banding in the short time limit.
2. Band coarsening in the long time limit.
3. Bands within bands for $n = 3$ frictional species.
4. Bands within bands, within bands for $n = 4$ frictional species; which varied when changes to the frictional properties were applied.

Finally, the number of bands formed with mill rotation rate suggests that there exists an optimal speed for recovering maximum number of bands. This is somewhere around 65% of critical speed.

There is certainly scope for future work. While the new free surface model is successful in its contribution towards banding and band coarsening, it certainly does not accurately match the measured free surface profile. The differences may be, in part, due to the use of lifter bars that have not been explicitly dealt with in this thesis. Suggested extensions should include the inertial number—A new dimensionless number recently argued by [4] as being suitable to granular systems. The constant bed depth assumption is also in disagreement with the PEPT data and should be modelled mechanistically, or at least semi-empirically. These limitations can be experimentally resolved by performing a complete experimental study of the proposed model. This was, unfortunately, outside the scope and budget of the present work.

Appendix A

Axial Segregation Derivations

A.1 The Diffusion Equation

The flux in the flowing layer is given by:

$$J = \frac{n\rho g}{3\eta} h^3 \cos\theta \left[\tan\theta - \mu\right]. \tag{A.1}$$

The height h (the depth of the flowing layer) can be obtained from the relation that describes the hydrostatic pressure in an inclined plane and is given by:

$$P_0(h) = \rho g h_0 \cos\theta \Longrightarrow h_0 = \frac{P_0}{\rho g \cos\theta},$$

where the depth is small compared to the radius of the drum. Eq. A.1 then becomes:

$$J = \frac{n\rho g}{3\eta} \left[\frac{P_0}{\rho g}\right]^3 \frac{1}{\cos^2\theta} \left[\tan\theta - \mu\right].$$

Using:

$$\frac{1}{\cos\theta} = \sec\theta \quad \text{and} \quad \sec^2\theta = 1 + \tan^2\theta$$

$$\Longrightarrow J = \frac{n}{3\eta} \frac{P_0^3}{(\rho g)^2} \left[1 + \tan^2\theta\right] \left[\tan\theta - \mu\right].$$

The multi-directional gradient is denoted as:

$$\tan\theta = \bigtriangledown y(x,z) \equiv \bigtriangledown_y,$$

where $\bigtriangledown_y$ is the axial gradient operator. Accordingly, the flux in the flowing layer becomes:

$$J = An_d \left[1 + |\bigtriangledown_y|^2\right] [|\bigtriangledown_y| - \mu] |\hat{\bigtriangledown}_y, \tag{A.2}$$

where n_d is the number density of the granular materials, $\hat{\bigtriangledown}_y$ is the unit vector in the x and z direction and the constant $A = \left(\frac{1}{3\eta}\frac{P_0^3}{(\rho g)^2}\right)$. The second term of the total flux, is the back-flow flux F_b. This is the flow used to prevent particles from accumulating at end-walls of the drum. The term is given by:

$$F_b = n_d h \vec{v}_z. \tag{A.3}$$

The total flux, J_t, is the summation of these two terms and this corresponds to:

$$J_t = J_z + n_d h \vec{v}_z. \tag{A.4}$$

A.2 Continuity Equation

There exist a continuity equation (for each of the two components of the mixture) which can be expressed as:

$$\frac{\partial n_d}{\partial t} = \vec{\bigtriangledown}.\vec{j_t}. \tag{A.5}$$

The relative concentration (fractional density) C, of the particles of each species of the mixture, is related to the number density. The relationship can be defined as:

$$C = \frac{n_d}{n_o}, \tag{A.6}$$

where n_o is the total number of the particles at any given slice and this is assumed to be constant. If the relative concentration of the low friction material is C, then the relative concentration of the high friction material is $1 - C$ with number densities of n_ℓ and n_h respectively. Consequently,

$$C = \frac{n_\ell}{n_o} \quad \text{and} \quad (1 - C) = \frac{n_h}{n_o}.$$

Then Eq. A.5 can be split into two equations (for each of the two species of the binary mixture) as:

$$\frac{\partial}{\partial t}C = -\frac{\partial}{\partial z}\int_{surface}\left[\frac{j_{\ell z}}{n_0} + Chv_z\right].\hat{\bigtriangledown}_y \tag{A.7}$$

$$\frac{\partial}{\partial t}(1-C) = -\frac{\partial}{\partial z}\int_{surface}\left[\frac{j_{hz}}{n_0} + (1-C)hv_z\right].\hat{\nabla}_y \tag{A.8}$$

The integral is evaluated over the whole free surface of the slice, because we are interested in the flows going out and into the slice. Adding Eq. A.7 to Eq. A.8 gives an expression for hv_z:

$$hv_z = -\frac{(j_{\ell z} + j_{hz})}{n_0}.$$

Substituting into Equ.A.7 gives,

$$\frac{\partial C}{\partial t} = -\frac{1}{n_0}\frac{\partial}{\partial z}\int_{surface}\left[(1-C)\, j_{\ell z} - C j_{hz}\right].\hat{\nabla}_y. \tag{A.9}$$

Eq. A.2 was used to insert the details of the fluxes $j_{\ell z}$ and j_{hz} as follows:

$$(1-C)j_{\ell z} - Cj_{hz} = -(1-C)n_\ell A\left[1+\nabla_y^2\right]\left[\nabla_y - \mu_\ell\right] + Cn_hA\left[1+\nabla_y^2\right]\left[\nabla_y - \mu_h\right]. \tag{A.10}$$

But: $n_\ell = n_0 C$ and $n_h = n_0(1-c) \Longrightarrow$

$$(1-C)j_{\ell z} - Cj_{hz} = -(1-C)n_0CA\left[1+\nabla_y^2\right]\left[\nabla_y - \mu_\ell\right] + Cn_0(1-C)A\left[1+\nabla_y^2\right]\left[\nabla_y - \mu_h\right],$$

$$= -ACn_0(1-C)\left[1+\nabla_y^2\right]\left[\nabla_y - \mu_\ell - \nabla_y + \mu_h\right], \text{ and}$$

$$\left[(1-C)j_{\ell z} - Cj_{hz}\right] = -ACn_0(1-C)\left[1+\nabla_y^2\right](\mu_h - \mu_\ell). \tag{A.11}$$

Substituting Eq. A.11 into Eq. A.9 gives:

$$\frac{\partial C}{\partial t} = +\frac{1}{n_0}\frac{\partial}{\partial z}\int_{surface} An_0C(1-C)\left[1+\nabla_y^2\right]\left[\mu_h - \mu_\ell\right].\hat{\nabla}_y. \tag{A.12}$$

Since $y = y(x,z)$, the axial operator $\vec{\nabla}_y$ can be written as:

$$\vec{\nabla}_y = \frac{\partial y}{\partial x}\hat{x} + \frac{\partial y}{\partial z}\hat{z} = y_x\hat{x} + y_z\hat{z},$$

and the scalar product is:

$$\vec{\nabla}_y.\vec{\nabla}_y = y_x^2 + y_z^2. \tag{A.13}$$

The magnitude of this operator can be obtained as:

$$|\nabla_y| = \left[y_x^2 + y_z^2\right]^{\frac{1}{2}} = \left(y_x^2\left[1 + \frac{y_z^2}{y_x^2}\right]\right)^{\frac{1}{2}} = y_x\left[1 + \left(\frac{y_z}{y_x}\right)^2\right]^{\frac{1}{2}}. \tag{A.14}$$

Using the binomial expansion:

$$\mid \bigtriangledown_y \mid = y_x \left[1 + \frac{1}{2} \left(\frac{y_z}{y_x} \right)^2 - \frac{1}{8} \left(\frac{y_z}{y_x} \right)^4 + ... \right]. \tag{A.15}$$

Then, taking the approximation to the first order [7, 11]:

$$\mid \bigtriangledown_y \mid \simeq y_x \Longrightarrow \mid \bigtriangledown_y \mid^2 \simeq y_x^2. \tag{A.16}$$

Also:

$$\hat{\bigtriangledown}_y = \frac{\vec{\bigtriangledown}_y}{\mid \bigtriangledown_y \mid} \simeq \frac{y_x \hat{x} + y_z \hat{z}}{y_x} = \hat{x} + \left(\frac{y_z}{y_x} \right) \hat{z}. \tag{A.17}$$

The component of $\hat{\bigtriangledown}_y$ in $\hat{z}$ direction is:

$$\hat{\bigtriangledown}_y = \left(\frac{y_z}{y_x} \right). \tag{A.18}$$

Substitute Eq. A.16 for $\mid \bigtriangledown_y \mid^2$ and Eq. A.18 for $\hat{\bigtriangledown}_Y$ into Eq. A.12:

$$\frac{\partial C}{\partial t} \simeq A \left[\mu_h - \mu_\ell \right] \frac{\partial}{\partial z} \int_{surface} \left[C(1-C) \left[1 + y_x^2 \right] \left[\frac{y_z}{y_x} \right] \right] \hat{z} \tag{A.19}$$

$$\frac{\partial C}{\partial t} \simeq A \left[\mu_h - \mu_\ell \right] \frac{\partial}{\partial z} \left[C(1-C) \int_{surface} \left[1 + y_x^2 \right] \left[\frac{y_z}{y_x} \right] \right] \hat{z} \tag{A.20}$$

The derivative $\frac{\partial y}{\partial z}$ can be written through $C(z)$ as:

$$\frac{\partial y}{\partial z} = \frac{\partial y}{\partial C} \frac{\partial C}{\partial z} = y_C \frac{\partial C}{\partial z}. \tag{A.21}$$

Finally, the diffusion equation that describes axial segregation of granular binary mixture in rotating drum is given by: [1]:

$$\frac{\partial C}{\partial t} \simeq A \left[\mu_h - \mu_\ell \right] \left[\int_{surface} \left[1 + y_x^2 \right] \left[\frac{y_C}{y_x} \right] \right] \frac{\partial}{\partial z} \left[C(1-C) \frac{\partial C}{\partial z} \right], \tag{A.22}$$

where the diffusion coefficient (D_{coef}) is:

$$D_{coef} = A \left[\mu_h - \mu_\ell \right] \left[\left[1 + y_x^2 \right] \left(\frac{y_C}{y_x} \right) \right]. \tag{A.23}$$

[1] $\star$ the integral is at a given instant in time.
$\star$ During that instant in time, C can be taken out of the integration.

For segregation (demixing) to occur, this coefficient must be negative. The main challenge facing the surface flow model is the calculations of this complicated diffusion coefficient.

A.3 Diffusion Equation with Bagnoldian Free-Surface

In the previous section we derived the diffusion equation using the Newtonian free-surface, where the applied shear stress was the Newtonian viscous shear stress. In this section, we present the diffusion equation by applying the Bagnoldian free-surface. Replacing the density ρ with the number density n_d, the mass flux in the flowing layer is given by:

$$\phi_f = \frac{2n_d}{5\sqrt{A}} \left[\rho g h_0^5\right]^{\frac{1}{2}} \left[\cos\theta \left(\tan\theta - \mu\right)^{\frac{1}{2}}\right]. \tag{A.24}$$

Using:

$$\frac{1}{\cos\theta} = \sec\theta \quad \text{and} \quad \sec^2\theta = 1 + \tan^2\theta$$

$$\implies \phi_f = n_d B \left[\frac{\tan\theta - \mu}{\left(\tan^2\theta + 1\right)^{\frac{1}{2}}}\right]^{\frac{1}{2}}, \tag{A.25}$$

where the constant B is $\frac{2}{5\sqrt{A}} \left[\rho g h_0^5\right]^{\frac{1}{2}}$.
Again, once translational symmetry is broken:

$$\tan\theta = \vec{\bigtriangledown}_y = y_x\hat{x} + y_z\hat{z}$$

$$\vec{\phi_f} = \frac{nB\left(\mid \bigtriangledown_y \mid - \mu\right)^{1/2}}{\left[\mid \bigtriangledown_y \mid^2 + 1\right]^{1/4}} \hat{\bigtriangledown}_y. \tag{A.26}$$

Following the same argument for axial flux, material balance and continuity, it is again easy to show that:

$$\frac{\partial C}{\partial t} = -\frac{1}{n_0}\frac{\partial}{\partial z}\int_{slice} \left(\left[1 - C\right]\phi_{\ell z} - C\phi_{hz}\right).\hat{\bigtriangledown}_y. \tag{A.27}$$

Note that, $n_\ell = n_0 C$ and $n_h = n_0(1-C)$. One can then get an expression for $([1-C]\,\phi_{\ell z} - C\phi_{hz})$ as :

$$([1-C]\,\phi_{\ell z} - C\phi_{hz}) = -n_0 BC(1-C)\frac{\left[[\mid \bigtriangledown_y \mid -\mu_h]^{\frac{1}{2}} - [\mid \bigtriangledown_y \mid -\mu_\ell]^{\frac{1}{2}}\right]}{\left[(\mid \bigtriangledown_y \mid^2 + 1)^{\frac{1}{4}}\right]}$$

and Eq. A.27 becomes:

$$\frac{\partial C}{\partial t} = \frac{\partial}{\partial z}\int_{slice} BC(1-C)\frac{\left[[\mid \bigtriangledown_y \mid -\mu_h]^{\frac{1}{2}} - [\mid \bigtriangledown_y \mid -\mu_\ell]^{\frac{1}{2}}\right]}{\left[(\mid \bigtriangledown_y \mid^2 + 1)^{\frac{1}{4}}\right]}.\hat{\bigtriangledown}_y \tag{A.28}$$

Using the 1^{st} order approximation of axial gradient operator in a binomial expansion and substituting Eq. A.16 for $\mid \bigtriangledown_y \mid^2$ and Eq. A.18 for $\hat{\bigtriangledown}_y$ into Eq. A.28 yields:

$$\frac{\partial C}{\partial t} \simeq \frac{\partial}{\partial z}\int_{slice} BC(1-C)\frac{\left[[y_x - \mu_h]^{\frac{1}{2}} - [y_x - \mu_\ell]^{\frac{1}{2}}\right]}{\left[(y_x^2 + 1)^{\frac{1}{4}}\right]}\left[\frac{y_z}{y_x}\right]\hat{z} \tag{A.29}$$

Since the z-dependence only enters parametrically through C(z), then:

$$\frac{\partial y}{\partial z} = \frac{\partial y}{\partial C}\frac{\partial C}{\partial z} = y_C\frac{\partial C}{\partial z} \tag{A.30}$$

$$\frac{\partial C}{\partial t} \simeq \left[B\int_{slice}\frac{\left[[y_x - \mu_h]^{\frac{1}{2}} - [y_x - \mu_\ell]^{\frac{1}{2}}\right]}{\left[(y_x^2 + 1)^{\frac{1}{4}}\right]}\left[\frac{y_C}{y_x}\right]\right]\frac{\partial}{\partial z}\left[C(1-C)\frac{\partial C}{\partial z}\right] \tag{A.31}$$

As it will presented in Chapter 4, the numerical solution of Eq. A.31 reproduces axial segregation and band formation even if the drum is less than half filled. This situation agrees with the experiment and could not be obtained using Eq. A.22, where the calculated free-surface profile is obtained from applying a Newtonian shear stress.

A.4 Diffusion Equation with Approximation to the Second Order

By taking the second order approximation of the binomial expansion of the axial gradient operator ($\mid \bigtriangledown_y \mid$) shown in Eq. A.15, we obtained:

$$\mid \bigtriangledown_y \mid = y_x \left[1 + \frac{1}{2}\left(\frac{y_z}{y_x}\right)^2\right] = y_x \left[1 + \frac{y_z^2}{2y_x^2}\right] \tag{A.32}$$

$$\Longrightarrow \mid \bigtriangledown_y \mid^2 = y_x^2 \left[1 + \frac{y_z^2}{2y_x^2}\right]^2 = y_x^2 + y_z^2 + \frac{y_z^4}{4y_x^2}. \tag{A.33}$$

Then, the unit vector $\hat{\bigtriangledown}_y$ can be given as:

$$\hat{\bigtriangledown}_y = \frac{\vec{\bigtriangledown}_y}{\mid \bigtriangledown_y \mid} \simeq \frac{y_x\hat{x} + y_z\hat{z}}{y_x\left[1 + \frac{y_z^2}{2y_x^2}\right]} = \frac{\hat{x}}{\left[1 + \frac{y_z^2}{2y_x^2}\right]} + \left(\frac{y_z}{y_x}\right)\frac{1}{\left[1 + \frac{y_z^2}{2y_x^2}\right]}\hat{z}. \tag{A.34}$$

The z-component of $\hat{\bigtriangledown}_y$ is:

$$\hat{\bigtriangledown}_y = \left(\frac{y_z}{y_x}\right)\frac{1}{\left[1 + \frac{y_z^2}{2y_x^2}\right]}. \tag{A.35}$$

If Eq. A.33 is substituted for $\mid \bigtriangledown_y \mid^2$ and Eq. A.35 for $\hat{\bigtriangledown}_y$ then Eq. A.12 becomes:

$$\frac{\partial C}{\partial t} = +\frac{1}{n_0}\frac{\partial}{\partial z}\int_{surface} ACn_0(1-C)\left[1 + y_x^2 + y_z^2 + \frac{y_z^4}{4y_x^2}\right][\mu_h - \mu_\ell]\left(\frac{y_z}{y_x}\right)\frac{1}{\left[1 + \frac{y_z^2}{2y_x^2}\right]}. \tag{A.36}$$

From Eq. A.21 it follows that:

$$\frac{\partial C}{\partial t} = A\left[\mu_h - \mu_\ell\right]\left[\int_{surface}\left[1 + y_x^2 + y_z^2 + \frac{y_z^4}{4y_x^2}\right]\frac{1}{\left[1 + \frac{y_z^2}{2y_x^2}\right]}\left(\frac{y_C}{y_x}\right)\right]\frac{\partial}{\partial z}\left[C(1-C)\frac{\partial C}{\partial z}\right]. \tag{A.37}$$

Approximating the axial gradient operator to the second order in the binomial expansion, introduces the derivative $\frac{dy}{dz}$. The role of this derivative is important in real-world mixing processes, where it is difficult to achieve the initial homogeneous state. Realistically, there often exist concentration fluctuations in the free-surface layer. As presented in Chapter 5, the approximation of axial gradient operator to

second order, and accordingly the appearance of the $\frac{dy}{dz}$ derivative, contributes to the coarsening effect.

Eq. A.37 represents the diffusion equation with the Newtonian shear stress and the second order approximation of axial gradient operator in a binomial expansion. Following the same argument, one can obtain the diffusion equation with the Bagnoldain shear stress and the second order approximation of axial operator in a binomial expansion as follows,

- Substitute Eq. A.33 for $|\bigtriangledown_y|^2$ and Eq. A.35 for $\hat{\bigtriangledown}_y$ in Eq. A.28:
- Use Eq. A.21.
- Then we obtain the second order-Bagnoldian-diffusion equation which can be stated as:

$$\frac{\partial C}{\partial t} \simeq \left[B \int_{slice} \frac{\left[\left[\left[y_x + \frac{y_z^2}{2y_x}\right] - \mu_h\right]^{\frac{1}{2}} - \left[\left[y_x + \frac{y_z^2}{2y_x}\right] - \mu_\ell\right]^{\frac{1}{2}}\right]}{\left[\left(y_x^2 + y_z^2 + \frac{y_z^4}{4y_x^2} + 1\right)^{\frac{1}{4}}\right]} \frac{1}{\left[1 + \frac{y_z^2}{2y_x^2}\right]} \left[\frac{y_C}{y_x}\right] \right] \frac{\partial}{\partial z}\left[C(1-C)\frac{\partial C}{\partial z}\right] \tag{A.38}$$

Important note:
In order to include the parameters associated with the physics of the new rheology into Eq. A.38, the derivative y_x which represents the Bagnoldian free-surface profile, must be taken from the equivalent derivation of free-surface profile where these parameters were defined.

Bibliography

[1] P. G. de Gennes, "Granular matter: a tentative view," *Reviews of Modern Physics*, vol. 71, no. 2, pp. S374–S382, 1999.

[2] G. L. F. Boschini, K. Traina, S. Bontempi, J.-C. Remy, R. Cloots, and N. Vandewalle, "Measuring the flowing properties of powders and grains," *Powder Technology*, vol. 224, pp. 19–27, 2012.

[3] A. de Ryck, H. Zhu, S. Wu, A. Yu, and P. Zulli, "Numerical and theoretical investigation of the surface flows of granular materials on heaps," *Powder Technology*, vol. 203, pp. 125–132, 2010.

[4] G. MiDi, "On dense granular flows," *Eur. Phys. J*, vol. E, no. 14, pp. 341–365, 2004.

[5] I. Govender and T. Pathmathas, "A positron emission particle tracking investigation of the flow regimes in tumbling mills," *Journal of Physics D: Applied Physics*, vol. 50, p. 035601 (10pp), 2017.

[6] N. Bell, Y. Yu, and P. J. Mucha, "Particle-based simulation of granular materials," *Eurographics / ACM SIGGRAPH Symposium on Computer Animation*, vol. K. Anjyo, P. Faloutsos (Editors), 2005.

[7] O. Zik, D. Levine, S. G. Lipson, S. Shtrikman, and J. Stavans, "Rotationally induced segregation of granular materials," *Physical Review Letters*, vol. 73, no. 5, pp. 644–647, 1994.

[8] Y. Forterre and O. Pouliquen, "Granular flows," *Glasses and Grains, Progress in Mathematical Physics*, vol. 61, pp. 77–109, 2011.

[9] B. Andreotti, Y. Forterre, and O. Pouliquen, "Granular media between fluid and solid," *Cambridge University Press*, p. 5, 2013.

[10] I. Goldhirsch, "Kinetic and continum descriptions of granular flows," *Mechanics for New Millennium, Progress in Mathematical Physics*, pp. 345–358, 2002.

[11] D. Levine, "Axial segregation of granular materials," *Chaos*, vol. 9, p. 3, 1999.

[12] I. S. Aranson, L. S. Tsimring, and V. M. Vinokur, "Continuum theory of axial segregation in a long rotating drum," *Phys. Rev. E*, vol. 60, no. 2, pp. 1975–1987, 1999.

[13] R. Bagnold, "Experiments on a gravity free dispersion of large solid spheres in a newtonian fluid under shear," *Proc. R. Soc. Lond.*, vol. A, no. 255, pp. 49–63, 1954.

[14] S. Savage and K. Hutter, "The motion of a finite mass of granular material down a rough incline," *J. Fluid Mech.*, vol. 199, pp. 177–215, 1989.

[15] P. Jop, Y. Forterre, and O. Pouliquen, "A constitutive law for dense granular flows," *Nature*, vol. 441, pp. 727–730, 2006.

[16] H. Lee and J. Huang, "Kinetic theory based model of dense granular flows down inclined planes.," *Physics of Fluids*, vol. 24, p. 073303, 2012.

[17] F. Rietz and R. Stannarius, "Convection and segregation in a flat rotating sandbox," *New Journal of Physics*, vol. 14, p. 015001, 2012.

[18] Y. Forterre and O. Pouliquen, "Flows of dense granular media.," *Annu. Rev. Fluid Mech.*, vol. 40, pp. 1–24, 2008.

[19] G. Seiden and P. J. Thomas, "Complexity, segregation, and pattern formation in rotating-drum flows," *Rev. Mod. Phys.*, vol. 83, no. 4, pp. 1323–1365, 2011.

[20] F. Pignatel, C. Asselin, L. Krieger, I. C. Christov, J. M. Ottino, and R. M. Lueptow, "Parameters and scalings for dry and immersed granular flowing layers in rotating tumblers," *Physical Rev.*, vol. E, no. 86, p. 011304, 2012.

[21] R. H. Perry and D. W. Green, "Perry's chemical engineers' hand-book," *Mcgraw Hill Chemical Engineering Series, New York*, 1984.

[22] A. Santomaso, "Chemical engineering research & design," *ISSN: 0263-8762*, vol. 81, no. 12, pp. 936–945, 2003.

[23] A. Samadani and A. Kudrolli, "Angle of repose and segregation in cohesive granular matter," *http://arxiv.org*, vol. abs/cond-mat.soft, p. 0106572v1, 2011.

[24] S. B. Savage, "Disorder and granular media," *edited by D. Bideau and A. Hansen*, vol. (North Holland, Amsterdam), p. 255, 1993.

[25] O. Pouliquen and Y. Forterre, "Friction law for dense granular flows: application to the motion of a mass down a rough inclined plane," *Physical Rev.*, vol. E, p. 011304, 2012.

[26] S. R. de Silva, A. Dyrøy, and G. G. Enstad, "Segregation mechanisms and their quantification using segregation testers," *IUTAM Symposium on Segregation of Granular Flows: Solid Mechanics and its applications*, vol. 81, pp. 11–29, 2000.

[27] A. Bhateja, J. K. Singh, and I. Sharma, "Axial segregation in horizontally vibrated granular materials: A numerical study," *KSCE Journal of Civil Engineering*, vol. 13, no. 4, pp. 289–296, 2009.

[28] J. Johanson, "Predicting segregation of bimodal particle mixtures using the flow properties of bulk solids," *Pharmaceytial Technology Europe*, vol. 20, pp. 46–57, 1996.

[29] J. Carson and D. J. Goodwill, "Understanding and eliminating particle segregation problems," *Bulk Solids Handl.*, vol. 6, pp. 139–144, 1986.

[30] W. R. Ketterhagen, J. S. Curtis, C. R. Wassgren, and B. C. Hancock, "Modeling granular segregation in flow from quasi-three-dimensional, wedg-shaped hoppers," *Powder Technology*, vol. 179, pp. 126–143, 2008.

[31] K. Johanson, "Optimal blender choices," *3536 NW 97 th Blvd. Gainesville, FL 32606, Material Flow Solutions, Inc.*, vol. 2, no. A, 2008.

[32] E. D. Liss, S. L. Conway, J. A. Zega, , and B. J. Glasser, "Segregation of powders during gravity flow through vertical pipes," *Pharmaceutical Technology*, vol. Circle/eINFO, no. 65, p. 80, 2004.

[33] K. Johanson, "Food facts," *7010 NW 23 rd Way Suite A, Gainesville, FL, 32653, Material Flow Solutions, Inc.*, vol. 1, no. B, 2012.

[34] J. J. M. Jr, "Mechanical separation and materials handling," *Unit Operations Handbook. ISBN 978-0-8247-8670-0*, vol. 2, pp. CRC Press. 256–, 1992.

[35] S. D. Gupta, D. Khakhar, and S. Bhatia, "Axial segregation of particles in a horizontal rotating cylinder," *Chem. Eng. Sci.*, vol. 46, no. 5/6, pp. 1513–1517, 1991.

[36] M. Nakagawa, "Axial segregation of granular flows in a horizontal rotating cylinder," *Chem. Eng. Sci.*, vol. 49, pp. 2540–2544, 1994.

[37] K. M. Hill, A. Caprihan, and J. Kakalios, "Bulk segregation in rotated granular material measured by magnetic resonance imaging," *Phys. Rev. Lett.*, vol. 78, no. 1, pp. 50–53, 1997.

[38] N. Taberlet, M. Newey, P. Richard, and W. Losert, "On axial segregation in a tumbler: An experimental and numerical study," *Stat. Mech. Theory Exp.*, vol. P07013, 2006.

[39] N. Jain, D. V. Khakhar, R. M. Lueptow, and J. M. Ottino, "Self-organization in granular slurries.," *Phys. Rev. Lett.*, vol. 86, pp. 3771–3774, 2001.

[40] Y. Oyama, "Axial segregation of granular materials.," *Bull. Inst. Phys. Chem. Res. Jpn. Rept. 5 (Tokyo)*, vol. 18, p. 600 (in Japanese), 1939.

[41] M. B. Donald and B. Roseman, "Mixing and demixing of solid particles, part 1, mechanisms in a horizontal drum mixer.," *Br. Chem. Eng*, vol. 7, pp. 749–753, 1962.

[42] I. S. Aranson and L. S. Tsimring, "Dynamics of axial separation in long rotating drums," *Phys. Rev. Lett.*, vol. 82, no. 23, pp. 4643–4646, 1999.

[43] K. Choo, T. C. A. Molteno, and S. W. Morris, "Traveling granular segregation patterns in a long drum mixer," *Phys. Rev. Lett.*, vol. 79, no. 16, pp. 2975–2978, 1997.

[44] Z. S. Khan, W. A. Tokaruk, and S. W. Morris, "Oscillatory granular segregation in a long drum mixer," *Europhys. Lett.*, vol. 66, no. 6, p. 212, 2004.

[45] K. Hill, A. Caprihan, and J. Kakalios, "Bulk segregation in a rotating granular material measured by magnetic resonance imaging," *Phys. Rev. Lett.*, no. 50, 1997.

[46] M. Newey, J. Ozik, Meer, E. Ott, and W. Losert, "Band-in-band segregation of multidisperse granular mixtures," *Europhys. Lett.*, vol. 66, no. 2, p. 205, 2004.

[47] P. Cundall and O. Strack, "A discrete numerical model for granular assemblies," *Geotechnique*, vol. 29, pp. 47–65, 1979.

[48] F. Bertrand, L.-A. Leclaire, and G. Levecque, "Dem-based models for the mixing of granular materials," *Chem. Eng. Sci.*, vol. 60, pp. 2517–2531, 2005.

[49] H. G. Matuttis, S. Luding, and H. J. Herrmann, "Discrete element methods for the simulation of dense packings and heaps made of spherical and non-spherical particles," *Powder Technol.*, vol. 109, pp. 278–292, 2000.

[50] R. Chand, M. A. Khaskheli, A. Qadir, B. Ge, and Q. Shi, "Discrete particle simulation of radial segregation in horizontally rotating drum: Effects of drum-length and non-rotating end-plates," *Physica*, vol. A, no. 391, pp. 4590–4596, 2012.

[51] Z. Khan and S. Morris, "Subdiffusive axial transport of granular materials in a long drum mixer," *Phys. Rev. Lett.*, vol. 94, p. 4, 2005.

[52] K. M. Hill, D. V. Khakhar, J. F. Gilchrist, J. J. McCarthy, and J. M. Ottino, "Segregation-driven organization in chaotic granular flows," *Proc. Natl. Acad. Sci. U.S.A.*, vol. 96, p. 11701, 1999.

[53] S. W. Meier, D. A. M. Barreiro, J. M. Ottino, and R. M. Lueptow, "Coarsening of granular segregation patterns in quasi-two-dimensional tumblers," *Nature*, vol. 4, pp. 244–248, 2008.

[54] V. Frette and J. Stavans, "Avalanche-mediated transport in a rotated granular mixture," *Phys. Rev. E*, vol. 56, no. 6, pp. 6981–6990, 1997.

[55] J. Rajchenbach, "Flow in powders: From discrete avalanches to continuous regime," *Physical Review Letters*, vol. 65, no. 18, pp. 2221–2224, 1990.

[56] N. Taberlet, P. Richard, and E. J. Hinch, "S shape of a granular pile in a rotating drum," *Physical Review E*, vol. E, no. 73, pp. 050301(R)–1 050301(R)–4, 2006.

[57] M. Hawkeswortha, M. O'Dwyera, and J. Walkera, "positron camera forindustrial application," *Nuclear Instruments and Methods*, vol. A, no. 253, pp. 145–157, 1986.

[58] D. Parkera, C. Broadbentb, P. Fowlesc, M. Hawkeswortha, and P. McNeil, "Positron emission particle tracking - a technique for studying flow within engineering equipment," *Nuclear Instruments and Methods in Physics Research*, vol. 326, no. 3, pp. 592–607, 1993.

[59] R. Wildmann, J. Huntley, J.-P. Hansen, D. Parker, and D. Allen, "Single-particle motion in three dimensional vibrofluidised beds," *Phys. Rev. E*, vol. 62, pp. 3826–3835, 2000.

[60] K. Sichalwe, I. Govender, and A. Mainza, "Characterising porosity of multi-component mixtures in rotary mills," *Minerals Engineering*, vol. 24, pp. 276–281, 2011.

[61] J. Canny, "A computational approach to edge detection," *IEEE Transactions on Pattern Analysis and Machine Intelligence*, vol. PAMI-8, pp. 679–698, 1986.

[62] K. Yamane, M. Nakagawa, S. A. Altobeli, T. Tanaka, and Y. Tsuji, "Steady Particulate Flows in a Horizontal Rotating Cylinder," *Physics of Fluids*, vol. 10, pp. 1419–1427, 1998.

[63] R. Hogg and D. Feurstenau, "Power relationships for tumbling mills," *SME-AIME Transactions*, vol. 252, pp. 418–423, 1972.

[64] C. Harris, E. Schnock, and N. Arbiter, "Grinding mill power consumption," *Miner. Process. And technol. Rev.*, vol. 1, pp. 297–345, 1985.

[65] S. Morrell, "Prediction of grinding-mill power," *Transactions of the Institution of Mining and Metallurgy Section C: Mineral Processing Extraction and Metallurgy*, vol. 101, pp. C25–C32, 1992.

[66] A. Tordisilla and D. Arber, "Capturing the s in segregation: a simple model of flowing granular mixtures in rotating drums," *International Journal of Mathematical Education in Science and Technology*, vol. 36, no. 8, pp. 861–877, 2005.

[67] H. T. Chou and C. F. Lee, "Cross-sectional and axial flow characteristics of dry granular material in rotating drums," *Granular Matter*, vol. 11, pp. 13–32, 2009.

[68] C. M. Dury and G. H. Ristow, "Boundary effects on the angle of repose in rotating cylinders," *arxiv.org*, vol. cond-mat/9710127v3, pp. 1–10, 1998.

[69] G. H. Ristow, "Pattern formation in granular materials," *Springer Science and Business Media*, vol. ISBN 978-3-540-66701-8, pp. 102–, 2000.

[70] D. C. Rapaport, "Simulated three-component granular segregation in a rotating drum," *Phys. Rev. E*, vol. 76, p. 041302, 2007.